Fall 2014

Energy deposition into heavy gas plasma via pulsed inductive theta-pinch

Ryan Alan Pahl

ENERGY DEPOSITION INTO HEAVY GAS PLASMA VIA PULSED INDUCTIVE

THETA-PINCH

by

RYAN ALAN PAHL

A DISSERTATION

Presented to the Faculty of the Graduate School of the

MISSOURI UNIVERSITY OF SCIENCE AND TECHNOLOGY

In Partial Fulfillment of the Requirements for the Degree

DOCTOR OF PHILOSOPHY

in

AEROSPACE ENGINEERING

2014

Approved by

Dr. Joshua Rovey, Advisor
Dr. Carlos Castaño
Dr. Chris Grabowski
Dr. David Pommerenke
Dr. David Riggins

PUBLICATION DISSERTATION OPTION

This thesis or dissertation has been prepared in the form of three papers and formated according to Missouri S&T guidelines. The papers have been prepared in accordance with the Missouri S&T dissertation style. The paper entitled Comparison of Magnetic Probe Calibration at Nano and Millitesla Magnitudes was published in the journal *Review of Scientific Instruments* in January 2014. The second and third papers have been submitted to *IEEE Transactions on Plasma Science*. The second paper, Energy Analysis of a Pulsed Inductive Plasma through Circuit Simulation, was published in September 2014. The final paper was submitted in October 2014 and is currently under review with the title Effects of DC Preionization Voltage and Radial Location on Pulsed Inductive Plasma Formation.

ABSTRACT

The objective of this research is to study the formation processes of a pulsed inductive plasma using heavy gases, specifically the coupling of stored capacitive energy into plasma via formation in a theta pinch coil. To aid in this research, the Missouri Plasmoid Experiment Mk. I (and later Mk. II) was created.

In the first paper, the construction of differential magnetic field probes are discussed. The effects of calibration setup on $\dot{B}$ probes is studied using a Helmholtz coil driven by a vector network analyzer and a pulsed-power system. Calibration in a pulsed-power environment yielded calibration factors at least 9.7% less than the vector network analyzer.

In the second paper, energy deposition into various gases using a pulsed inductive test article is investigated. Experimental data are combined with a series RLC model to quantify the energy loss associated with plasma formation in Argon, Hydrogen, and Xenon at pressures from 10–100 mTorr. Plasma resistance is found to vary from 25.8–51.6 mΩ and plasma inductance varies from 41.3–47.0 nH. The greatest amount of initial capacitively stored energy that could be transferred to the plasma was 6.4 J (8.1%) of the initial 79.2 ± 0.1 J.

In the third paper, the effects of a DC preionization source on plasma formation energy is studied. The preionization source radial location is found to have negligible impact on plasma formation repeatability while voltage is found to be critical at low pressures. Without preionization, plasma formation was not possible. At 20 mTorr, 0.20 W of power was sufficient to stabilize plasma formation about the first zero-crossing of the discharge current. Increasing power to 1.49 W increased inductively coupled energy by 39%. At 200 mTorr, 4.3 mW was sufficient to produce repeatable plasma properties.

ACKNOWLEDGMENTS

First, I would like to thank my advisor, Dr. Joshua Rovey, for all your help and encouragement over the years. I've enjoyed our relationship both professionally and personally. This research has been, on the whole, very enjoyable and exciting, and none of it would have happened without you. Personally, how many advisors would scuba dive in the middle of a frigid October in Rolla so that I could get certified in underwater pumpkin carving? You can be confident that no one else on the planet can claim that honor.

I'd also like to thank Drs. Carlos Castaño, David Pommerenke, and David Riggins for serving on my committee. Dr. Pommerenke and his student Guanghua Li's help was invaluable while working on probe design and calibration. Dr. Riggins, I've thoroughly enjoyed all the classes I've taken from you over the years.

Chris, I'd like to especially thank you for all your tutelage these past two years and for serving on my committee. My experience with FRCHX has been invaluable to my research. The creation of MPX Mk. II was a direct result of what I learned from you. Your various equipment loans and donations helped make this research possible. And a special thanks to Dr. William White for giving me the chance to work with AFRL.

I would like to thank my family and friends for their support over the years. Mom and Dad, thanks for raising me over the years. The values you two taught me allowed me to get to where I am today.

As tradition, I wish to also thank my fellow "top grad students" in the APLab. Warner, our numerous and unnecessarily long discussions effectively killed productivity on a near daily basis. Paul, your cleaver reasoning and logical deduction lead to one of the greatest insights in APLab history: "it's because of the plasma". Steve, your great conversational skills has turned "meh" into the most versatile word in the english language. Kapton, you were the silent hero that held the lab together.

TABLE OF CONTENTS

SECTION

LIST OF ILLUSTRATIONS

LIST OF TABLES

1. INTRODUCTION

1.1. MOTIVATION

Historically, manned space exploration has been limited to the confines of near-Earth missions. Food, water, and transit times present significant challenges that inhibit mankind from pushing farther into space. In order to address and overcome these challenges, advanced propulsion concepts need to be found that provide significant performance increases over today's space propulsion capabilities.

Pulsed plasma systems show great potential for future space propulsion systems. However, knowledge gaps in the formation process of heavy-gas plasma present significant hurdles that must be overcome for the technology to be fully realized. This work is focused on elucidating the fundamental mechanisms associated with heavy-gas break-down in a cylindrical pulsed-power theta-pinch device. Specifically, a pulsed inductive test article using a cylindrical theta-pinch coil is designed and constructed to produce plasmas of interest for interrogation. Calibration techniques of magnetic field probes are explored in detail to address probe error associated with variations between calibration and pulsed-power environments. Models are developed in SPICE and fit to experimental discharge current profiles to quantify the energy deposited into the plasma by the discharge circuit. Plasma modeling is further refined with the use of axial plasma imaging and an axial array of radially aligned photomultiplier tubes enabling the determination of plasma thickness and the interval of time for which plasma is present. Effects of a DC preionization source voltage and radial location on plasma formation and energy coupling is also investigated. Once total energy deposited into the plasma is determined, future work can endeavor to identify and quantify internal plasma loss mechanisms such as excitation, ionization, wall transport, etc. By studying the loss mechanisms and temporal energy evolution profiles

associated with pulsed-inductive discharges, current models can be improved to better aid the design of an advanced plasma propulsion device.

1.2. INDUCTIVELY COUPLED PLASMA

Inductively Coupled plasmas (ICPs) are, most generally, neutral gas that has been ionized by strong electromagnetic fields produced by driving large currents through an inductive coil. The inductors have no rigidly defined geometry but typically fall into one of three categories:

1. cylindrical $(\theta = 0^{\circ})$

2. conical $(0^{\circ} < \theta < 90^{\circ})$

3. planar $(\theta = 90^{\circ})$.
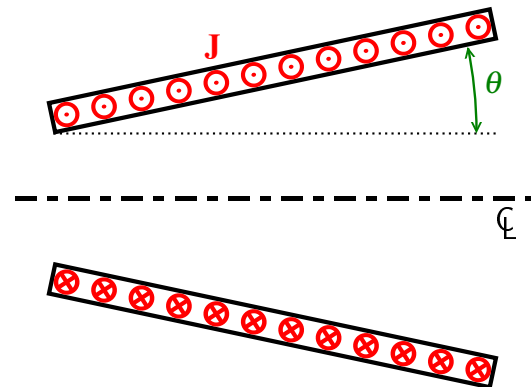
Figure 1.1. Inductor geometry variations relative to half-angle θ.

Large discharge current is achieved by charging a capacitor bank to high voltage and quickly discharging this energy through the inductive coil. The discharge current $\vec{I}$ is distributed through the coil with current density $\vec{J}$ (Eq.(1.1)). This azimuthal current sheet produces axial magnetic fields within the coil through Ampère's Law (Eq.(1.2)) which then gives rise to a radially varying azimuthal electric field by Faraday's Law (Eq. (1.3)). When a quasi-neutral gas is present, the electric field accelerates unbounded charged particles producing a diamagnetic current within the device. The accelerated charged particles collide with neutrals resulting in either excited species or ionization. This process is typically

dominated by electron-neutral collisions due to the increased mobility of the electrons relative to ions which have a larger mass. For devices with small half-angles, the axial magnetic field confines or "pinches" the plasma giving rise to the name θ-pinch. Figure 1.2 illustrates the basic device physics of an ICP.

$$\vec{I} = \iint_S \vec{J} \cdot d\vec{S} \tag{1.1}$$

$$\oint_C \vec{B} \cdot d\vec{\ell} = \mu_0 \iint_S \left(\vec{J} + \varepsilon_0 \frac{\partial \vec{E}}{\partial t} \right) \cdot d\vec{S} \tag{1.2}$$

$$\vec{\nabla} \times \vec{E} = -\frac{\partial \vec{B}}{\partial t} \tag{1.3}$$
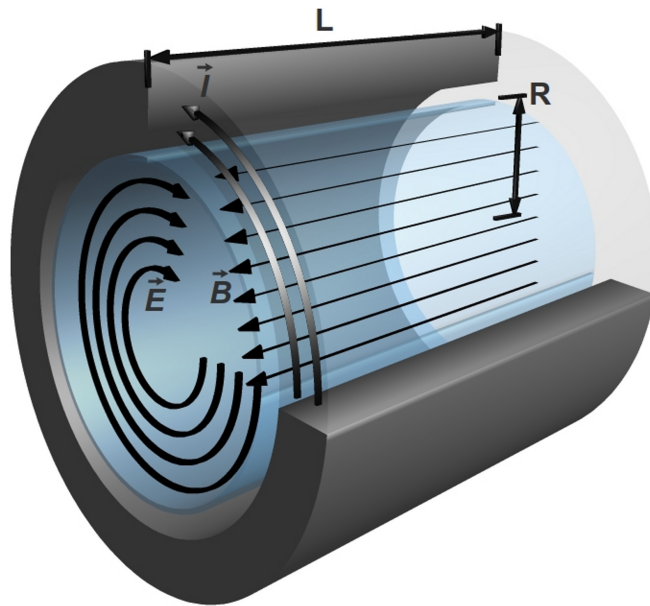
Figure 1.2. Physics of an inductively coupled plasma.

1.2.1. Compact Toroid. A Compact Toroid (CT) is defined by a closed magnetic field structure, independent of the magnetic field of the inductive coil that originally formed

the plasmoid. [**?**] This characteristic allows for CTs to have relatively high plasma β (Eq. (1.4)) such that the plasma pressure is balanced by the magnetic pressure ($\beta \approx 1$).

$$\beta = \frac{nk_{\mathrm{B}}T}{B^2/2\mu_0} \tag{1.4}$$

The qualities of magnetic detachment and radial confinement initially spurred interest in CT plasmas in the fusion community for D-D and D-T reactors and was later adopted by the spacecraft community as a potential high-power propulsion system using heavier gases such as Argon and Xenon.

1.2.2. Field Reversed Configuration. Field Reversed Configurations (FRCs) are one subset of the compact toroid (CT) family of ICPs and is of interest to the propulsion community. Tuszewski [**?**] wrote an extensive review on the state of FRC research in 1988 and Steinhauer [**?**] provided an update on the status of FRCs to include recent achievements in the field. However, for completeness, a brief overview of FRCs is provided for the reader.

FRCs are characterized by relatively strong poloidal magnetic fields and little or no toroidal magnetic fields ($B_{\mathrm{z}} \gg B_\theta$). FRCs are formed by applying a magnetic field in the reverse direction of a preexisting field. Typically this is achieved by establishing a reverse bias magnetic field prior to discharge of the main capacitor banks, although early experiments succeeded using only a main bank discharge. [**?**]

1.2.3. FRC Formation. Other authors describe the FRC formation process in more detail [**?**], but a basic diagram illustrating the various stages has been reproduced from Ref. [**?** , Fig. 3] and presented in Fig. 1.3. Neutral gas is fed into a non-conductive insulator, typically quartz, and a bias field is applied through the use of permanent magnets or a pulsed circuit with a discharge frequency much lower than that of the main discharge circuit. The gas is ionized and charged particles orbit magnetic field lines of the bias field effectively "freezing" the bias field into the plasma. The discharge current in the theta-
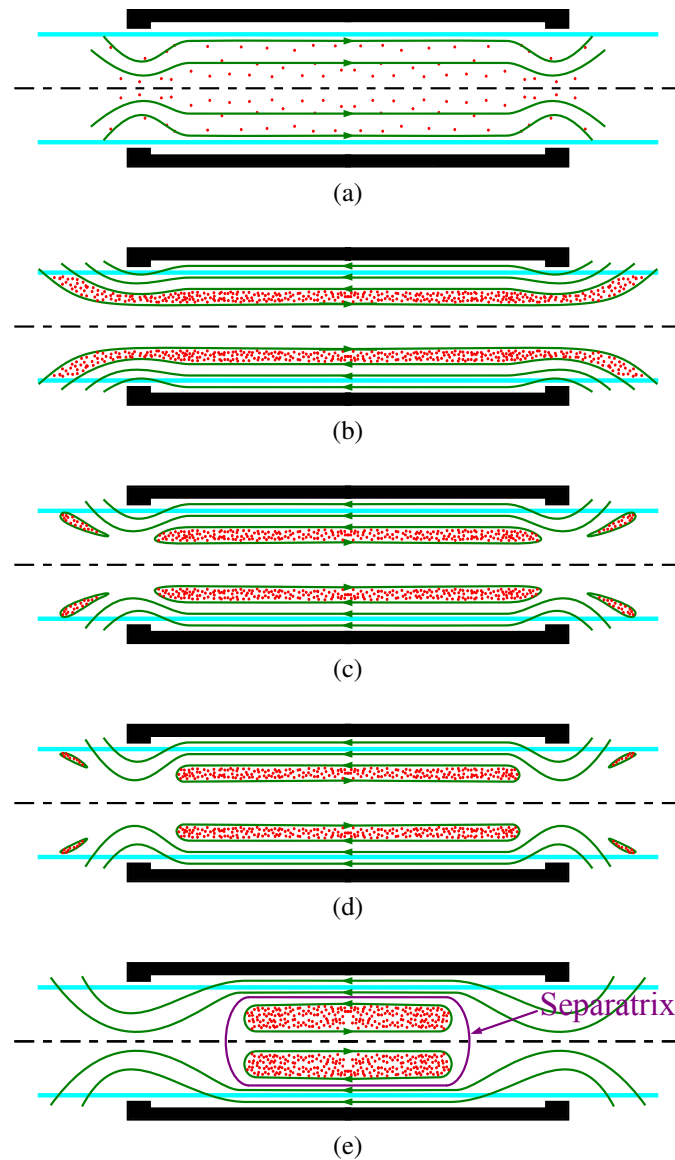
Figure 1.3. Stages of FRC formation. (a) Bias field applied and plasma ionized. (b) Applied magnetic field is reversed relative to bias field. (c) Plasma is radially compressed and plasma field lines "tear" and reconnect. (d) Plasma undergoes axial contraction. (e) Equilibrium reached and separatrix fully established.

pinch coil is then quickly reversed. The increased diffusion time of the magnetic field into the plasma results in opposing field lines at the boundary of the plasma volume. The resulting electromagnetic forces produce a radially inward $(-\hat{r})$ force, compressing the plasma. Increased current densities at the edge of the theta-pinch produce larger field magnitudes re-

sulting in a magnetic mirror which causes plasma field lines to "tear" away from field lines of the coil and reconnect to adjacent plasma field lines near the center of the plasmoid. The plasma then experiences axial contraction in addition to additional radial compression until an equilibrium is reached ($\beta \cong 1$). [**?**]

1.2.4. Pulse Inductive Thruster Research. The Pulsed Inductive Thruster (PIT) was one of the earliest inductive plasma accelerators (1965) and helped lay the foundation for modern pulse inductive thrusters. Initial work focused on current sheet microstructure of a planar accelerator and the plasma acceleration mechanism. [**?**] Results with a 20 cm diameter accelerator showed a specific impulse (I_{sp}) of 1500 s and an efficiency of 11% when operating on argon. Significant improvements in I_{sp} and efficiency were achieved with a later 1 m diameter accelerator design. An (I_{sp}) of 2240 s at 50% energy efficiency was measured for a 7.5 mg impulse bit for a 4 kJ discharge (20 μF at 20 kV) in argon. [**? ?**] Tests with the PIT MkV produced (I_{sp})s of 2000–8000 s with efficiencies between 42–52% and a nominal impulse bit of 0.1 N-s. [**? ?**]

The Faraday Accelerator with Radio-frequency Assisted Discharge (FARAD) [**? ? ? ? ? ? ?**] incorporated a RF (13.56 MHz) helicon antenna prior to a planar coil to preionize propellant before main discharge. Using RF preionization, FARAD produced inductive current sheets with a discharge energy of 44 J at 1.5 kV, substantially lower than 4 kJ necessary for PIT. Difficulties "turning" the ionized gas 90° to disperse over the planar surface lead to the development of the Conical Theta Pinch FARAD (CTP-FARAD). [**? ?**] Initial results indicate that increasing gas pressure eliminates non symmetries present in current sheets formed at low gas pressures.

1.2.5. FRC Research. FRCs for space propulsion application have been previously investigated at the University of Washington, University of Alabama-Huntsville, and at the Air Force Research Laboratory (AFRL) at Edwards Air Force Base. [**? ? ? ? ? ? ? ?**] These studies have mainly focused on lower energy FRC formation and translation with higher atomic mass gases.

Research performed at the University of Washington has investigated the use of FRCs for space propulsion and fusion, both individually and as a combined spacecraft system. Slough, et.al., have investigated the Propagating Magnetic Wave Plasma Accelerator (PMWAC) device for space propulsion [? ?] and also an earth-to-orbit fusion plasmoid device. [?] Both of these have similar operating principles. First, a FRC is created. Then the FRC is accelerated using a magnetic wave created by a sequence of pulsed electromagnetic coils. If the device is only providing propulsion, then the accelerated FRC is expelled at high velocity. However, if fusion is desired, then the FRC is compressed to smaller diameter causing the temperature to increase to fusion levels. Power can then be extracted for use creating the next FRC and the process is repeated. Results showed an ejection velocity of at least 1.8×10^5 m/s for each deuterium plasmoid, which yielded a total impulse bit of 0.3 N-s.[?]

The University of Washington in collaboration with MSNW LLC is also developing the Electrodeless Lorentz Force (ELF) thruster. The goal of the ELF device is to demonstrate efficient acceleration of a variety of propellants to high velocities (10–40 km/s) and operation at high power (e.g. > 100 kW). The device is designed around a conical geometry with a rotating magnetic field current drive to ionize the gas and drive an azimuthal current to form an FRC. [?]

Investigations at the University of Alabama-Huntsville and NASA Marshall Space Flight Center have centered on the Plasmoid Thruster Experiment (PTX) which uses a conical rather than cylindrical geometry. [? ? ? ?] This geometry has benefits because the FRC creation and acceleration occur within the same step. Unlike the PMWAC developed by Slough, a traveling magnetic wave is not required to accelerate the FRC. Results have shown electron temperature and density of 7.6 eV, and 5.0×10^{13} cm^{-3} for argon and 23 eV and 1.2×10^{14}cm^{-3} for hydrogen.[?] Exit velocities up to 2.0×10^4 m/s have been measured.

The electric propulsion group at Edwards Air Force Base constructed an annular FRC device called XOCOT. [**?**] The XOCOT project primary goal was to develop FRC-based plasmas at low power with long lifetime for propulsion applications. The program investigated different charging energies, voltages, and timing, as well as multiple propellants and pre-ionization techniques. Results showed multiple plasma formation and implosions are possible with densities and electron temperature on the order of $3.0 \times 10^{13} \mathrm{cm}^{-3}$ and 8 eV, respectively. [**?**] Current Air Force efforts in collaboration with Michigan Technological University are focused on understanding and quantifying the acceleration mechanism, plume profile, and plume energy of an FRC thruster.[**?**] XOCOT-T, the most recent version of the XOCOT experiment, is focused on the translation of FRCs formed at low voltages (0.5–3.0 kV) on longer time scales. This is accomplished with the use a three-turn conical outer coil and a pulsed gas puff valve. Several pressures and gas puff lengths have been investigated to determine optimal formation conditions. [**?**]

1.3. DISSERTATION ORGANIZATION

This dissertation is organized primarily around the publication of three journal articles. Calibration of magnetic field probes was published in Review of Scientific Instruments and can be found in Sec. 6. Development and implementation of a circuit model in SPICE for determination of temporal evolutions of plasma energies is presented in Sec. 6 and was published in IEEE Transactions on Plasma Science. Analysis of DC preionization source voltage and radial location on plasma formation repeatability and improved circuit modeling has been submitted to IEEE Transactions on Plasma Science and can be found in Sec. 6. Final conclusions are presented in Sec. 3.

2. EXPERIMENTAL SETUP

2.1. MISSOURI PLASMOID EXPERIMENT

A significant portion of this research involved the design, construction, and testing of a pulsed-power test article capable of forming a plasma in addition to the development and implementation of numerous diagnostics. The Missouri Plasmoid eXperiment (MPX) uses a cylindrical theta-pinch to inductively form plasma. Two variations of MPX were constructed during the course of this research. The first iteration, MPX Mk. I, used a 0.16 cm thick plate of copper that was rolled into a 17.8 cm diameter 76.2 cm long cylinder with two 12.7 cm tabs at the cylinder gap. To reduce parasitic inductances, the coil was mounted directly to the top of the 707 nF discharge capacitor with a GP-14B spark gap installed between the coil and the capacitor anode. The assembled configuration of MPX Mk. I is shown in Fig. 2.1. Additional information regarding MPX Mk. I can be found in Refs. [**? ? ?**].
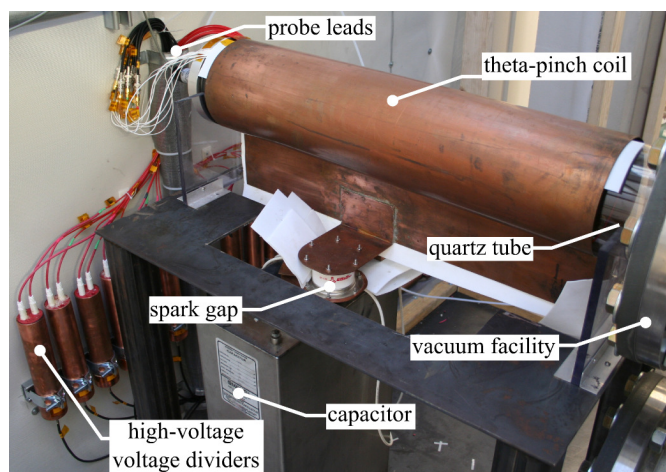
Figure 2.1. Missour Plasmoid eXperiment Mk. I. Theta-pinch coil constructed from single piece of rolled copper plate and mounted directly to the discharge capacitor to minimize line lengths and reduce losses.

The second iteration of MPX (Mk.II) was modeled after the theta-pinch coil used in AFRL's Field Reversed Configuration Heating eXperiment (FRCHX). The copper coil was replaced with an eleven-segment coil constructed from aluminum 7075 donated by The Boeing Company to the Missouri S&T Department of Mechanical and Aerospace Engineering. The segments are constructed in symmetric halves and then bolted together with two threaded rods. The segments are precision machined to have an ID of exactly 17.78 ± 0.01 cm, an improvement over the Mk. I coil which suffered from a non-uniform diameter as a result of the rolling process. Four axial threaded rods are used to align the assembled segment halves with nylon spacers placed between segments allow for probe leads to be relieved radially. Radial relief of probe leads reduced the electromagnetic compatibility issues encountered in the Mk. I design which ran the probe leads axially along the quartz tube under the theta-pinch coil.

Relevant dimensions of the quartz tube and MPX Mk. I and II are given in Table 2.1. Solid model drawings of the Mk. II design and probe layout are shown in Figs. 2.2 and 2.3. Assembled coil is presented in Figs. 2.4 and 2.5. Final MPX Mk. II integrated into the Aerospace Plasma Laboratory Space and High-Altitude Environment Testing Facility at Missouri S&T is shown in Fig. 2.6. Additional information regarding MPX Mk. II can be found in Refs. [**? ? ?**]

Table 2.1. Dimensions of MPX Mk. I and Mk. II experiments.

Property	Quartz Tube		Mk. I		Mk. II	
Material	214 Quartz		Copper		Aluminum	
Number of Turns	N/A		1		1	
Number of Segments	N/A		1		11	
Inner Diameter [mm (in)]	154.5	(6.1)	178	(7.0)	178	(7.0)
Outer Diameter [mm (in)]	161.0	(6.3)	181	(7.1)	N/A	
Thickness [mm (in)]	3.06	(0.12)	1.59	(0.06)	N/A	
Length [mm (in)]	915	(36.0)	762	(30.0)	783.5	(30.8)
Inductance [nH]	N/A		37.2		36.2	
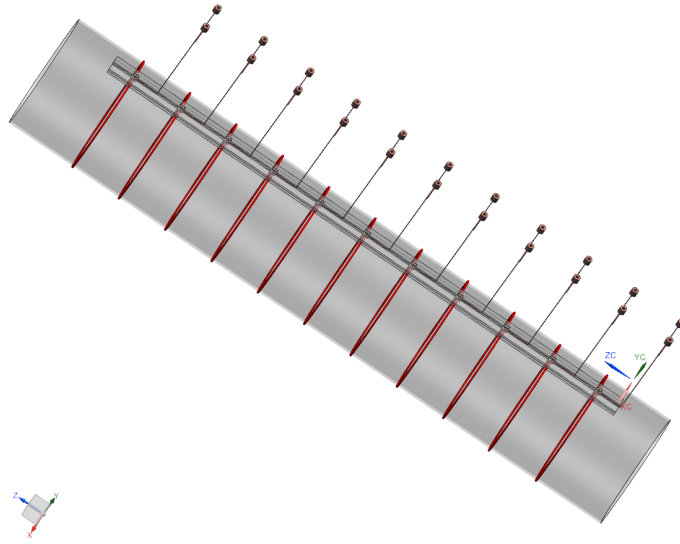
Figure 2.2. Axial probe array of eleven $\dot{B}$ probes and flux loop pairs.
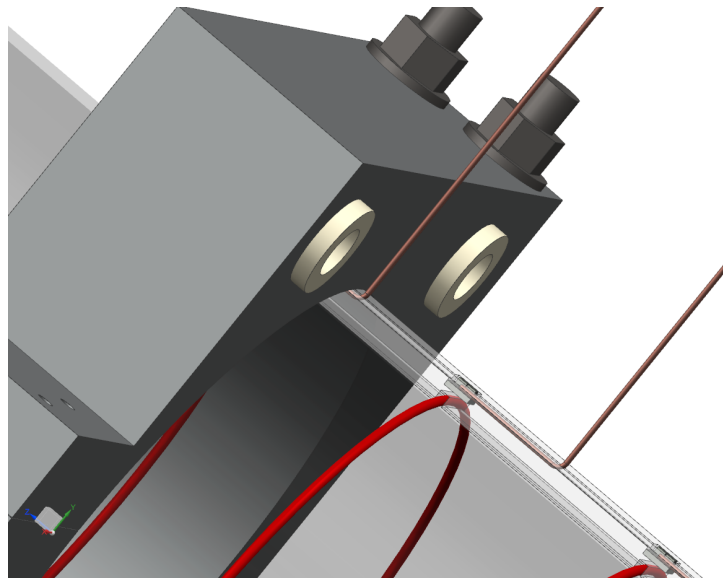
Figure 2.3. Integration of $\dot{B}$ probe and flux loop under coil segment with radial relieved leads
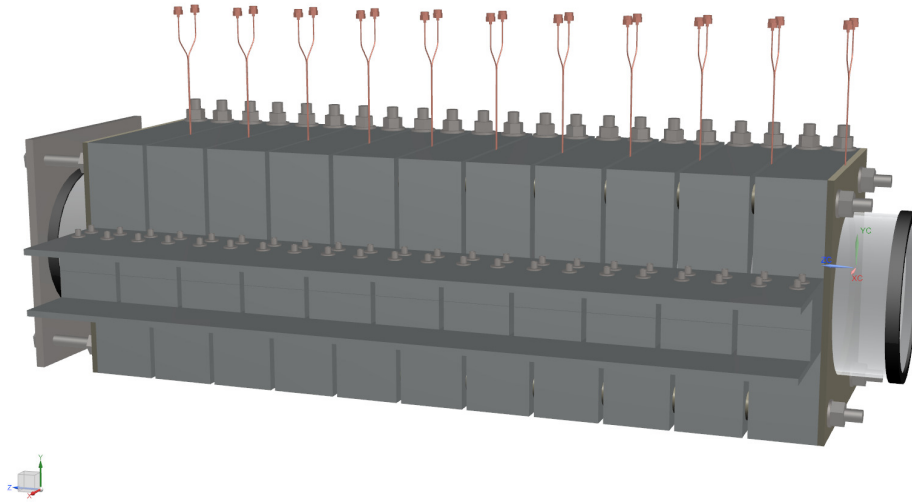
Figure 2.4. MPX Mk. II fully integrated coil and probe array.
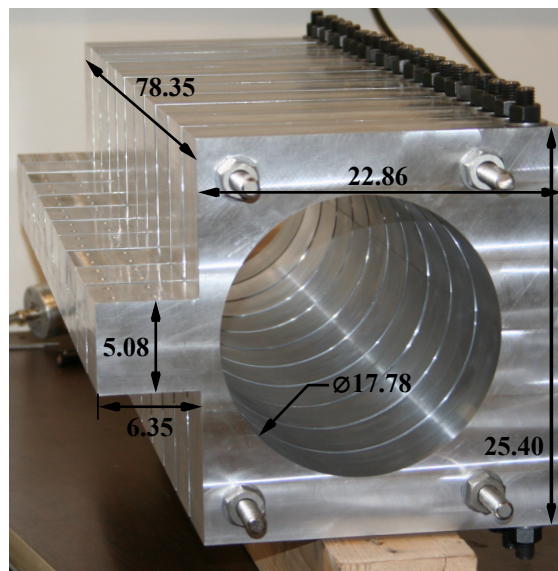
Figure 2.5. MPX Mk. II integrated coil segments. All dimensions in centimeters.

2.2. VACUUM PUMPING SYSTEM AND GAS FLOW CONTROLLER

2.2.1. Space & High-Altitude Environment Testing Facility. Testing was conducted at The Space & High-Altitude Environment Testing Facility located in the Aero-
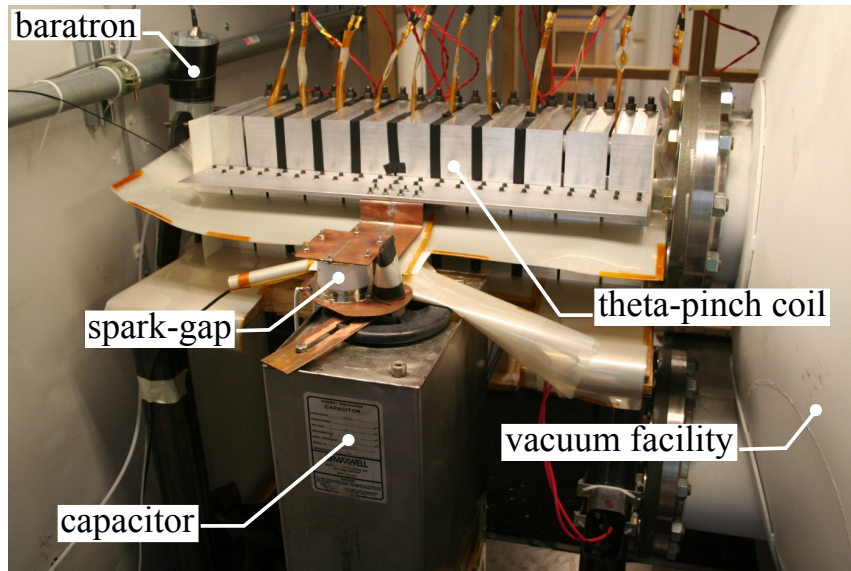
Figure 2.6. Missouri Plasmoid eXperiment Mk. II.

space Plasma Laboratory at Missouri S&T. The 1.8 m diamter 3.0 m long vacuum chamber uses four 0.89 m Varian NHS-35 diffusion pumps to provide the high throughput required by large propulsion systems. Each pump has a rated throughput of 50,000 L/s on air, 62,500 L/s on helium. The diffusion pumps are backed by an Edwards EH 4200 roots blower and a Tokuda KP-7500BG rotary vane pump. A total of ten 40.6 cm flanges are installed on the vacuum chamber: three are located on each end of the chamber while two are located on both the top and bottom of chamber. The facility is shown in Fig. 2.7.

2.2.2. Flow Controller. An Alley Cat MC20 flow controller is used to back fill MPX with various propellants. The flow controller can provide flow rates up to 20 sccm with an accuracy of $\pm 1.0\%$ for species of interest: argon, xenon, and hydrogen.

2.2.3. Pressure Gauges. The primary diagnostic for measuring vacuum chamber base pressure is a cold cathode Pirani ACC 2009 full range gauge capable of measuring pressure from 3.8×10^{-6} mTorr to 750 torr with an accuracy of $\pm 30\%$ and repeatability of $\pm 5\%$. An Extorr XT100 Residual Gas Analyzer is used to detect various gas species constituents and is used to detect system leaks.
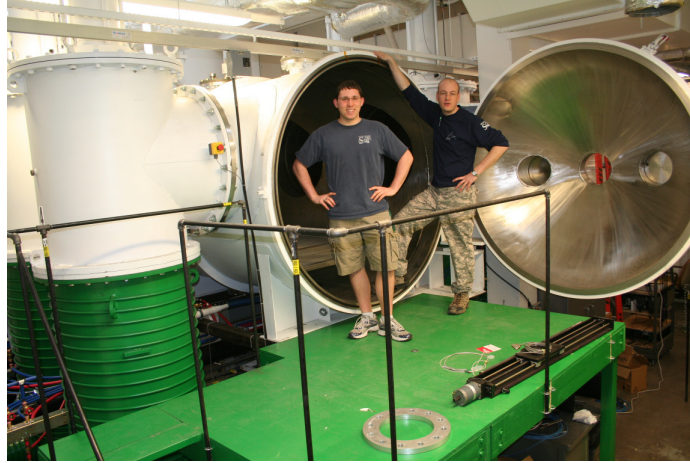
Figure 2.7. Aerospace Plasma Laboratory Space & High-Altitude Environment Testing Facility at Missouri S&T. Ryan Pahl (author) left, Warner Meeks right.

A high accuracy (0.5%) MKS model 626 Baratron gauge connected to a MKS PDR2000 dual capacitance manometer display is used to measure the fill pressure of MPX during testing for pressures of 0.01–100 mTorr. For pressures greater than 100 mTorr, a Varian 0531 thermocouple guage connected to a Kurt J. Lesker KJLC 615 display is provides pressure readings from 1–2000 mTorr with an accuracy of 10%.

2.3. DATA ACQUISITION

The data acquisition system for MPX utilizes the National Instruments (NI) PXI platform. A PXI 1000-B modular chassis houses a PXI-8336 PXI-PCI fiber optic communications module for PC control of the PXI system and provides optical isolation for safety. Six PXI-5105 modules are used for data acquisition and provide 48 channels of simultaneously collected data with 12-bit vertical resolution at 60 MS/s. A custom LabVIEW program was created that synchronizes the individual cards and allows the user to configure channel properties independently (i.e., vertical scale, input impedance, etc.). Each channel uses 50Ω cabling with a 50Ω external termination at the scope to reduce experiment noise resulting from the pulsed power environment. All probe leads are run through steel elec-

trical conduit to provide additional shielding against external signals. The data acquisition system is shown in Fig. 2.8.

Figure 2.8. Data acquisition system.

PAPER

I. COMPARISON OF MAGNETIC PROBE CALIBRATION AT NANO AND MILLITESLA MAGNITUDES

Ryan A. Pahl, Joshua L. Rovey, and David. J. Pommerenke

Missouri University of Science and Technology, Rolla, Missouri, 65401, USA

ABSTRACT

Magnetic field probes are invaluable diagnostics for pulsed inductive plasma devices where field magnitudes on the order of tenths of Tesla or larger are common. Typical methods of providing a broadband calibration of $\dot{B}$ probes involve either a Helmholtz coil driven by a function generator or a network analyzer. Both calibration methods typically produce field magnitudes of tens of microTesla or less, at least three and as many as six orders of magnitude lower than their intended use. This calibration factor is then assumed constant regardless of magnetic field magnitude and the effects of experimental setup are ignored. This work quantifies the variation in calibration factor observed when calibrating magnetic field probes in low field magnitudes. Calibration of two $\dot{B}$ probe designs as functions of frequency and field magnitude are presented. The first $\dot{B}$ probe design is the most commonly used design and is constructed from two hand-wound inductors in a differential configuration. The second probe uses surface mounted inductors in a differential configuration with balanced shielding to further reduce common mode noise. Calibration factors are determined experimentally using an 80.4 mm radius Helmholtz coil in two separate configurations over a frequency range of 100 – 1000 kHz. A conventional low magni-

tude calibration using a vector network analyzer produced a field magnitude of 158 nT and yielded calibration factors of $15\,663 \pm 1.7\%$ and $4920 \pm 0.6\%$ $\frac{\text{T}}{\text{V·s}}$ at 457 kHz for the surface mounted and hand-wound probes, respectively. A relevant magnitude calibration using a pulsed-power setup with field magnitudes of 8.7 to 354 mT yielded calibration factors of $14\,615 \pm 0.3\%$ and $4507 \pm 0.4\%$ $\frac{\text{T}}{\text{V·s}}$ at 457 kHz for the surface mounted inductor and hand-wound probe, respectively. Low-magnitude calibration resulted in a larger calibration factor, with an average difference of 9.7% for the surface mounted probe and 12.0% for the hand-wound probe. The maximum difference between relevant and low magnitude tests was 21.5%.

1. INTRODUCTION

Magnetic field ($\dot{B}$) probes are commonly used in pulsed inductive plasma (PIP) devices to measure time-varying magnetic fields. [**?** **?** **?** **?** **?** **?** **?** **?** **?**] In these pulsed systems, energy is initially stored as electrical energy in capacitor banks. During discharge, this energy is converted to electrical and magnetic fields to breakdown a neutral gas. Two common PIP device applications are nuclear fusion and spacecraft propulsion. Fusion devices such as the Z-Machine at Sandia National Laboratories [**?**] and the Field Reversed Configuration Heating Experiment (FRCHX) [**?**] at the Air Force Research Laboratories at Kirtland AFB use several MJ of energy per pulse to produce magnetic fields on the order of Teslas and even as large as 250 T [**?**] for magnetically-confined fusion. Propulsion systems operate at lower energies, using as little as one joule [**?**] and up to a few kJ of stored energy per pulse to produce magnetic fields on the order of tenths of a Tesla. [**?**]

In its simplest form, a $\dot{B}$ probe consists of a segment of wire formed into a closed geometric shape, typically a circle. Per Faraday's law, when placed in the presence of a time-varying magnetic field, a voltage is induced in the loop of wire proportional to the time-varying magnetic field. A brief overview of the $\dot{B}$ probe theory is provided in Ref. [**?**]. The two calibration methods accepted by the Institute of Electrical and Electronics Engineers (IEEE) for calibration of $\dot{B}$ probes are the Helmholtz coil and Transverse Electromagnetic (TEM) cell. [**?**] Helmholtz coils are commonly used due to their ease of construction and large area of field uniformity. [**?**] In a cylindrical region spanning $0.3r$ axially and $0.3r$ radially from the center of the Helmholtz coil, field uniformity varies less than 1%. [**?**] Additionally, Helmholtz coils can often accommodate larger field magnitudes than TEM cells but have lower operational frequencies. [**?**]

Calibration of $\dot{B}$ probes presents a few challenges. The first challenge is the dependence of the probe sensitivity on frequency. Because the probe head is an inductor,

the probe output voltage will attenuate when driven at higher frequencies as a result of increased probe reactance. Messer et al. provide a more complete analysis of $\dot{B}$ probe sensitivity and incorporate effects of transmission lines on probe response. [?] An additional challenge arises when using a Helmholtz coil as a calibration source. The inductance of the coil windings preclude driving large currents at frequencies of interest for pulsed inductive plasma due to increased impedance at increased frequencies reducing the calibration field magnitude. Consequentially, calibration of $\dot{B}$ probes are often performed at relevant frequencies but not relevant field magnitudes.

Field magnitudes on the order of 10 μT or less are often used to calibrate probes intended to measure field magnitudes of 10 mT or greater. In Ref. [?], the primary experiment is expected to generate fields of 18 mT at 59 kHz. However, calibration is accomplished with a field magnitude three orders of magnitude less than the intended field magnitude. Similarly, Ref. [?] performs probe calibrations in a Helmholtz coil with a maximum field magnitude of 60 μT. An experimental field magnitude is not explicitly given, however, the author cites plasma experiments such as fusion studies and inductively coupled plasmas as the common applications which have fields often greater than 10 mT.

This work quantifies the error associated with the assumption of a constant calibration factor when using low-magnitude fields to calibrate $\dot{B}$ probes intended for PIP devices. Two different $\dot{B}$ probe configurations are used and their construction outlined in section 2. Two different setups are used to produce low and relevant magnetic fields for calibration of the $\dot{B}$ probes and are presented in section 3. Initial results are presented in section 4 with a detailed analysis presented in section 5. Final conclusions are presented in section 6.

2. PROBE CONSTRUCTION

Special care must be observed in the construction of $\dot{B}$ probes for application in PIP devices due to the presence of large field magnitudes. In particular, the capacitive coupling due to fluctuations in electrostatic potentials can produce significant probe voltages that obscure the desired inductive signal and produce significant measurement error. [?] This problem is further exacerbated by the presence of plasma in PIP devices. One solution to this challenge is to use a $\dot{B}$ probe in a differential configuration. Differential probes use two identical $\dot{B}$ probes to remove the electrostatic coupling. This is possible because inductive pickup (differential mode) is dependent on the orientation of the probe in the magnetic field and capacitive pickup (common mode) remains unchanged with probe orientation. By using two identical probes with one oriented $180°$ relative to the second, subtracting the resulting signals removes the capacitive pickup and doubles the inductive pickup. The work by Franck et al. analyzes the electrostatic rejection of the most common differential probe configurations. [?] Work done by Loewenhardt et al. suggests that a center tapped configuration yields an order of magnitude reduction in capacitive pickup relative to a simply wound magnetic probe and therefore both probes in this study employ a center tapped configuration. [?]

Two $\dot{B}$ probe variations were constructed for the purposes of this study. The first is a configuration commonly used when constructing $\dot{B}$ probes and consists of two sets of ten turns of number 32 American Wire Gauge (AWG) enameled copper (magnet) wire wrapped around a 4.88 mm diameter dowel rod. The magnet wire has a polyester insulation with a polyamideimide overcoat and conforms to the ANSI/NEMA MW-35C/73C standards. The 32 AWG wire has a diameter of 0.23 mm, yielding a mean probe diameter of 5.11 mm. This gives a nA (turns-area) constant of 205×10^{-6} turns-m^2. The probe calibration factor from Faraday's law is defined as the inverse of the nA constant, giving a theoretical probe calibration factor of 4876 $\frac{\text{T}}{\text{V·s}}$. Terminating the probe into a 50 Ω load

necessitates doubling the probe sensitivity giving 9770 $\frac{T}{V \cdot s}$ into 50 Ω. Each probe head has approximately 177 mm of twisted leads that are then connected to twelve centimeters of RG-58/U coaxial cable and terminated with SMA connectors. The second probe design uses two Coilcraft 1008CS-102XFLB surface mounted inductors (SMIs). The inductors have a rated tolerance of 1% with a self inductance of 963 nH at 1 MHz and a self resonant frequency of 290 MHz. The manufacture provided nA constant of 154×10^{-6} turns-m^2 gives a theoretical calibration factor of 6494 $\frac{T}{V \cdot s}$ or 12987 $\frac{T}{V \cdot s}$ into 50 Ω. The SMIs are soldered to a custom printed circuit board with two 22.8 cm leads constructed of 1.2 mm diameter semi-rigid coaxial cable and terminated with SMA connectors. Shielding of inductive probes has been well studied [? ? ?] and has been shown to reduce the electrostatic noise on the probe. A good example of an electrostatically shielded probe is presented by Biloiu et al. [?] For additional shielding, the SMI probe is wrapped in a single layer of copper tape. Solder is used to secure the copper tape to the probe and electrically connect the shield to the ground conductor of the semi-rigid coaxial cables. A gap is added to the center of the shield structure on the back of the probe head. This balances and thus cancels currents generated by the electrostatic noise on the probe shield. Figure 2.1 shows a comparison of the two probes in this study. The SMI is shown prior to the addition of the copper tape shielding.
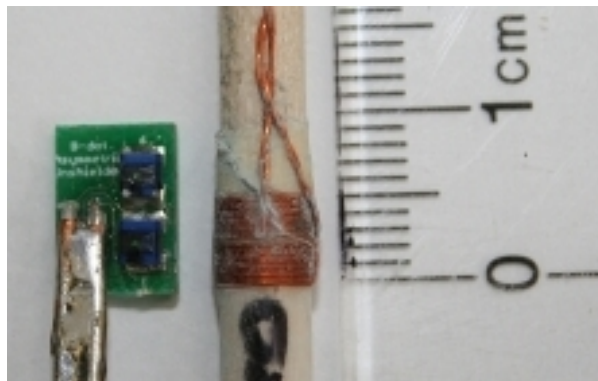
Figure 2.1. Photo showing SMI (left) and hand-wound probe (right) for comparison.

3. EXPERIMENTAL SETUP

Two experimental setups are used in this work. First, a network analyzer is used to provide a low magnitude frequency domain calibration. This is one of the most commonly employed calibration setups and can produces fields as high as tens of μT (dependent on Helmholtz coil geometry) over a wide range of frequencies. The second method uses a pulsed-power RLC discharge at high voltage at select frequencies to provide relevant field magnitudes at select relevant frequencies. The same Helmholtz coil, probe cables, and attenuators are used for both calibration setups. The only change was replacing the high voltage capacitor and spark gap with the network analyzer. This minimizes the impact that the test setup has on the results.

The single-turn loops of the Helmholtz coil used in testing are constructed of a one turn aluminum ring with a cross-section of 6.0 mm $\times$ 6.4 mm. Measured from the center of the ring cross-sections, the diameter of the Helmholtz coil is 160.8 mm and the distance between the rings is 80.7 mm. A large non-conductive slug is placed in the center of the Helmholtz coil to ensure probe placement remains constant within the Helmholtz field. The machined probe holder ensures that the sensing region of the probe is perpendicular to the center axis of the probe holder. The larger slug then ensures that the probe holder is axially aligned at the center of the Helmholtz field. A test of the Helmholtz field uniformity is performed and compared to simulations in EMC Studio [**?**] with results shown in Fig. 3.1. Helmholtz theory predicts a peak field of 221.9 mT at 39.7 kA current for a discharge frequency of 88 kHz. Simulation gives a max field of 219.6 mT, a percent difference of 1.06%.

3.1. LOW MAGNITUDE CALIBRATION

An Agilent Technologies E5071C network analyzer was used to perform low magnitude frequency domain measurements from 100 – 1000 kHz. Sweeps were conducted
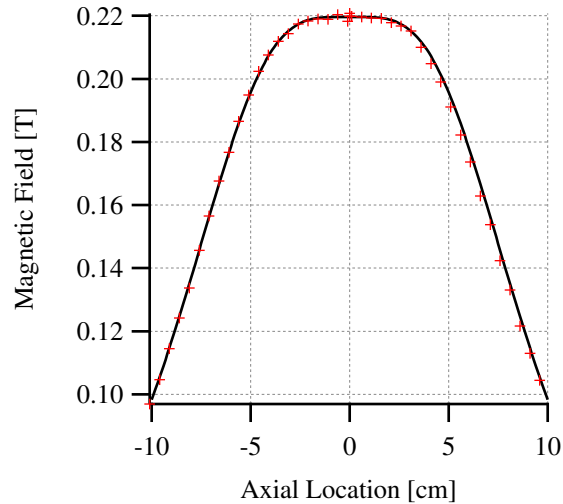
Figure 3.1. Comparison of measured Helmholtz coil field to simulation conducted in EMC Studio. Experimental data collected with the hand-wound probe using the pulsed power setup at 13 kV and 88 kHz.

with a 30 Hz filter and results averaged over two tests. The output power was set at the maximum 10 dBm. Calibration of the network analyzer was performed prior to testing using a Hewlett Packard 85033D 3.5 mm calibration kit. The network analyzer produced a driving current of approximately 28.3 mA into the Helmholtz coil resulting in a field magnitude of 158.2 nT.

3.2. RELEVANT MAGNITUDE CALIBRATION

PIP devices typically have fields greater than 10 mT. To achieve magnetic fields on that order of magnitude, a pulsed power RLC circuit was used. To achieve discharges at multiple frequencies, multiple capacitor banks were used in combination with two different series inductors. Table 3.1 lists the combination of capacitor and inductor values used and the resulting discharge frequency. Galvanized steel with a width of 80 mm and a thickness of 1.2 mm was used as transmission line in the experiment. An EG&G GP-41B triggered spark gap was used as the switch in the RLC circuit. A Pearson 1049 current monitor was

Table 3.1. Capacitance and inductance values used in generating relevant magnetic fields for calibration of Ḃ probe.

| Frequency [kHz] | | Capacitance | Inductance |
Target	Actual	$[\mu F]$	$[\mu H]$
50	50	1.005	9.40
100	88	7.190	0.00
100	98	0.275	9.40
250	240	1.005	0.00
500	457	0.275	0.00
750	799	0.056	0.00
1000	1089	0.027	0.00

used to measure the discharge current with a rated accuracy of +1/-0%. The 9.4 μH inductor used to modify discharge frequency was constructed by wrapping ten turns of 12 AWG magnet wire around a section of 89 mm diameter PVC pipe. To prevent arcing, a winding pitch of 4.2 mm was used and the inductor was potted in epoxy to hold the coil shape during testing. Using the method outlined by Lundin [?], the calculated inductance of the Helmholtz coil was 268 nH. Modeling in SPICE [?] indicates the parasitic capacitance to be less than one percent of the total circuit capacitance value. The stray inductance of the circuit is approximately 200 nH. Per IEEE std 1309-2005, the Helmholtz coil must be operated in a volume with a minimum radius of 6.7r, where r is the Helmholtz coil radius, devoid of conductors which may perturb the field geometry. [?] For electrical shielding of the high field magnitude tests, the Helmholtz coil was placed in a cylindrical metal enclosure with a radius of 0.91 m and a length of 3.0 m.

3.3. DATA ACQUISITION

All data in the relevant magnitude calibration were acquired using a PXI-5105 12-bit digitizer. The probes were connected to two 6.1 m RG-400/U cables. The two cables were extended horizontally from the centerline axis of the Helmholtz coil away from the

probes. After 0.61 m (as per the 6.7r requirement) the cables enter rigid conduit to provide additional shielding in the pulsed-power environment as the probe leads are brought outside of the shielded enclosure. Each probe lead then enters two Bird 25-A-MFN-10 attenuators connected in series to provide 20 dB total signal attenuation. A 33 cm long section of RG-223/U cable brings the signal to the PXI-5105 digitizer where they are terminated with external 50 Ω terminators. The Pearson 1049 output signal is treated similarly, however the conduit covers the full length of transmission line inside the shielded enclosure as the current monitor is sufficiently far from the Helmholtz coil and does not violate the 6.7r requirement.

4. RESULTS

This section presents the results of the low magnitude and relevant magnitude calibrations. Results from the low magnitude testing are presented in section 4.1 while relevant magnitude results are presented in section 4.2.

4.1. LOW MAGNITUDE CALIBRATION

Calibration factors from the low magnitude magnetic field tests using the dual port network analyzer are determined by converting scatter parameters from frequency domain to time domain for direct comparison to relevant magnitude tests. This is accomplished by using the S_{11} reflection parameter to determine the coil inductance and driving current over the tested frequency domain. The voltage induced on the $\dot{B}$ probe on channel 2 by driving the Helmholtz coil on channel 1 is calculated from the S_{21} transmission parameter. The resulting calibration factors are presented in Table 4.1 at the same frequencies

Table 4.1. Results from low magnitude frequency domain Helmholtz calibration.

Frequency [kHz]	Probe Calibration Factor $\left[\frac{T}{V \cdot s}\right]$	
	SMI	Hand-Wound
100	$15\,411 \pm 7.2\%$	$4860 \pm 1.7\%$
240	$15\,510 \pm 2.2\%$	$4883 \pm 0.8\%$
457	$15\,663 \pm 1.7\%$	$4920 \pm 0.6\%$
799	$15\,905 \pm 0.8\%$	$4977 \pm 0.3\%$
1000	$16\,047 \pm 0.8\%$	$5010 \pm 0.2\%$

that are used for the relevant magnitude calibrations. Calibration factors are calculated by averaging the results of the A and B halves of the probes and applying a linear fit to the

data. The resulting linear regressions calculated for the SMI and hand-wound probes are $k_{\mathrm{SMI}} = 15\,340 + 0.708f$ and $k_{\mathrm{HW}} = 4843.3 + 0.167f$, respectively, where f is the frequency in kHz. Reported uncertainty is calculated by averaging the deviation from the linear regression of the ten points to the left and to the right of the frequency of interest. Hardware limitations of the network analyzer limited the lowest frequency to 100 kHz, slightly higher than either the 88 or 98 kHz used in the relevant magnitude calibration. Calculations for converting the network analyzer results to time domain calibration factors are presented in the Appendix. At 100 kHz, the measured probe inductances are 1.14 μH and 0.85 μH for the SMI and hand-wound probes, respectively, and .95 μH and 0.68 μH at 1000 kHz. The measured SMI inductance differs from manufacture provided values of 0.96 μH at 1000 kHz by only 1.6%.

4.2. RELEVANT MAGNITUDE CALIBRATION

For relevant magnitude calibration, the magnitude of the magnetic field is calculated using the Helmholtz equation,

$$B_{\mathrm{H}}(t) = \left(\frac{4}{5}\right)^{\frac{3}{2}} \frac{\mu_0 n I(t)}{r} \tag{4.1}$$

where μ_0 is the permeability of free space, n is the number of turns of wire per coil, I is the current, and r is the radius of the Helmholtz coil. The Helmholtz field in Eq. 4.1 is calculated using the current measured from the Pearson current monitor. The pulsed power circuit used discharge voltages ranging from 13 to 23 kV to provide a range of relevant field magnitudes for calibration of the $\dot{B}$ probes. Table 4.2 provides the peak magnetic field obtained for a given frequency at a specified discharge voltage. Using the peak magnetic field values given in Table 4.2 and the corresponding peak of the integrated $\dot{B}$ signal, a calibration factor was calculated.

Table 4.2. Peak magnetic fields produced during relevant magnitude testing for a given discharge voltage.

Frequency [kHz]	Peak Magnitude [mT] (Discharge Voltage [kV])	
	Minimum	Maximum
50	21.5 (13)	35.5 (21)
88	245 (13)	354 (18)
98	10.8 (13)	18.3 (21)
240	84.8 (13)	131 (19)
457	43.5 (13)	83.0 (23)
799	14.4 (13)	25.3 (21)
1089	8.7 (13)	16.4 (21)

Five tests were performed at each field magnitude for a given frequency and calibration values for a given discharge frequency are averaged over the voltage domain tested. The standard deviation is reported as the probe uncertainty. The resulting calibration values are shown in Table 4.3.

Table 4.3. Results from relevant magnitude time domain Helmholtz calibration.

Frequency [kHz]	Probe Calibration Factor $\left[\frac{T}{V \cdot s}\right]$	
	SMI	Hand-Wound
50	14 532±0.6%	4529±0.8%
88	14 566±0.1%	4482±0.1%
98	14 374±1.5%	4385±5.4%
240	14 459±0.4%	4476±0.3%
457	14 615±0.3%	4507±0.4%
799	14 352±0.7%	4412±2.2%
1000	13 408±2.4%	4123±3.1%

5. ANALYSIS

Low magnitude calibration results in larger calibration factors than relevant magnitude calibration. The percent difference between relevant magnitude and low magnitude calibration factors is shown in Table 5.1 (relative to the relevant magnitude). The 100 kHz

Table 5.1. Percent difference of relevant magnitude and low magnitude calibration factors for SMI and hand-wound probes.

Frequency [kHz]	Percent Difference [%]	
	SMI	Hand-Wound
88	5.8±7.7	8.4±2.0
98	7.2±10	10.8±8.4
240	7.3±2.8	9.1±1.2
457	7.2±2.1	9.2±1.0
799	10.8±1.7	12.8±2.9
1089	19.7±3.9	21.5±4.2
Avg.	9.7±4.6	12.0±3.3

low magnitude calibration factor is used for both the 88 and 98 kHz relevant magnitude comparison, and the 1000 kHz low magnitude calibration factor is used for the 1089 kHz relevant magnitude comparison. The average percent difference between low magnitude and relevant magnitude calibration factors is $9.7 \pm 4.6\%$ and $12.0 \pm 3.3\%$ for the SMI and hand-wound probes, respectively.

In relevant magnitude testing, the largest variations in calibration factors were observed at frequencies where the common mode component of the signals was most substantial. At 50 kHz, the hand-wound probe measured a 19.8 V common mode signal, 13 times larger than the 1.52 V differential signal. The hand-wound probe measured common mode signals at least 570% greater than the differential mode signal for the 50, 98, and 1000 kHz

tests and equivalent signal magnitudes at 799 kHz. The SMI probe experienced lower ratios of common mode to differential mode signals: 1.3 at 50 kHz and 1.2 at 98 kHz. The SMI probe recorded lower common mode voltages and common mode to differential mode ratios than the hand-wound probe at all frequencies. The SMI probe recorded common mode voltages of one volt or less for all frequencies except 240 kHz. These low common mode signals contribute to the lower measurement uncertainty for the SMI probe compared to the hand-wound probe at relevant magnitude tests. This illustrates the necessity of shielding $\dot{B}$ probes in the high-noise environments encountered in PIP devices. The addition of a balanced shield on the SMI probe resulted in substantially less common mode noise.

Linear regressions of frequency domain probe response data yield slopes of 19.6 and 19.7 $\frac{\text{dB}}{\text{decade}}$ for the hand-wound and SMI probes, respectively, compared to the ideal response of 20 $\frac{\text{dB}}{\text{decade}}$. Correlation to the data is poor at low frequencies do to large uncertainties and produces the non-ideal response. Time domain tests exhibited non-ideal behavior at 799 and 1089 kHz. Rather than increasing with frequency, the calibration factors of the SMI and hand-wound probes decrease after 457 kHz. Based on the Helmholtz Equation (Eq. 4.1), there are two possibilities: reduction in current magnitude or increased probe response due to noise. Calibration of the current monitor indicates the sensitivity only varied by 1.8% over the frequency domain tested. This suggests that the decrease in $\dot{B}$ calibration factors at 799 and 1089 kHz is primarily due to a probe response above what a purely differential signal should produce. Fitting linear regressions to the data from 88 to 457 kHz, approximations to a theoretical calibration factor can be extrapolated. From the extrapolated results, the common mode signal contributed an additional 2.5% and 9.4% to the calibration factor at 799 and 1089 kHz, respectively, for the SMI probe compared to 3.6% and 11.1% for the hand-wound probe. Furthermore, the presence of unmitigated common mode noise explains the trend that all relevant magnitude calibration tests produced smaller calibration factors than those calculated at low magnitude. This further highlights

the need to calibrate probes in an environment similar to the environment of the primary experiment.

6. CONCLUSIONS

Calibration of two different magnetic fields probes at low (158.2 nT) and relevant (8.7 – 354 mT) field magnitudes at relevant frequencies of 100 to 1000 kHz for pulsed inductive plasmoid devices are presented. Calibration at relevant magnetic field magnitudes resulted in a lower calibration factor than low magnitude tests and increased measurement uncertainty at higher frequencies. Calibration at low magnitudes may produce an "absolute" calibration but it leaves the experimenter ignorant of potential signal contributions from common mode sources which may obscure the intended differential field measurement significantly at relevant magnitudes. In this work, despite the efforts taken to enhance probe and cable shielding and mitigate common mode signals, average variations between relevant and low magnitude tests still yielded a variation of $9.7 \pm 4.6\%$ for the SMI probe and $12.0 \pm 3.3\%$ for the hand-wound probe. An experimentalist using a typical hand-wound $\dot{B}$ probe can expect errors greater than 10.0% at low frequencies (less than 500 kHz for the probes tested) and greater than 20% at higher frequencies (1000 kHz or greater) if common the mode contribution is not quantified when operating in a pulsed-power environment.

ACKNOWLEDGMENTS

APPENDIX

VNA CONVERSION CALCULATIONS

Both the source (R_S) and load (R_L) impedance is assumed to be 50 Ω. To determine the current in the Helmholtz coil, the input power must be converted from dBm to Watts using Eq. 1 and the S reflection and transmission parameters converted from dB to magnitudes using Eq. 2.

$$P = 10^{\frac{\text{dBm}-30}{10}} \tag{1}$$

$$|S_{xy}| = 10^{\frac{S_{xy}\,[\text{dB}]}{20}} \tag{2}$$

The complex form of S_{xy} is calculated using Eq. 3

$$S_{xy} = |S_{xy}|e^{j\theta_{xy}} \tag{3}$$

where θ_{xy} is the phase of the S_{xy} parameter in radians. Finally, the S_{xy} parameter is converted to a complex impedance using Eq. 4.

$$Z_{xy} = R_S \frac{1 + S_{xy}}{1 - S_{xy}} \tag{4}$$

From the complex impedance, the Helmholtz coil inductance can be calculated using the complex impedance calculated from S_{11}.

$$L_{\text{Helm}} = \frac{\text{Im}(Z_{11})}{\omega} \tag{5}$$

Using the power and source impedance, the source voltage output from the network analyzer can be calculated.

$$V_S = 2\sqrt{PR_S} \tag{6}$$

Using the source voltage and source resistance with the Helmholtz coil inductance, the driving current can be calculated.

$$I_C = \frac{V_S}{R_S + j\omega L} \tag{7}$$

Finally, the Helmholtz equation is used to determine the magnetic field.

$$B_{\text{Helm}} = \left(\frac{4}{5}\right)^{\frac{3}{2}} \frac{\mu_0 n I_C}{r} \tag{8}$$

The probe response is calculated in Eq. 9 using the reflection parameter S_{21}.

$$V_R = |S_{21}|\sqrt{PR_L} \tag{9}$$

In time domain, the probe response is typically integrated as shown in Eq. 10.

$$a = \int_0^t V(t')\mathrm{d}t', 0, t \tag{10}$$

An identity of the Fourier Transform allows for the same operation to be performed in frequency domain:

$$\text{FFT}(a) = \text{FFT}\left(\int_0^t V(t')\mathrm{d}t', 0, t\right) = \frac{V_R}{j\omega} \tag{11}$$

Finally the calculated magnetic field is divided by the probe response to get the calibration factor.

$$k = \left|\frac{B_H}{a}\right| \tag{12}$$

II. ENERGY ANALYSIS OF A PULSED INDUCTIVE PLASMA THROUGH CIRCUIT SIMULATION

Ryan A. Pahl and Joshua L. Rovey

Missouri University of Science and Technology, Rolla, Missouri, 65401, USA

ABSTRACT

Current profiles of a cylindrical ringing theta-pinch are compared to SPICE simulations of an established circuit model and a least squares estimate is performed to determine plasma resistance and inductance for argon, hydrogen, and xenon plasmas with prefill pressures ranging from 10–100 mTorr. Plasma resistance is found to vary from 25.8–51.6 mΩ with the lowest resistance occurring at 10 mTorr. Argon and xenon follow a similar trend with the xenon resistance averaging 4.2 mΩ (12.3%) larger than argon from 40–100 mTorr. Hydrogen resistance is found to increase rapidly as prefill pressure increases above 40 mTorr. Calculated plasma resistivity of 214–429 Ω-μm agrees with established literature. Plasma inductance varies from 41.3–47.0 nH and is minimized at 30 mTorr for argon and hydrogen while xenon inductance is minimized at 20 mTorr. Hydrogen yields the highest inductance, averaging 1.9 nH (4.5%) more than argon over the pressure range tested. Temporal evolution of the energy partitioning into capacitive, inductive, and resistive loads is presented. Plasma inductive energy is found to be maximized when discharge current reaches its peak negative value of -23.5 kA. Xenon shows the greatest amount of inductive energy storage with a peak of 6.4 J (8.1%) of the initial 79.2 ± 0.1 J while argon dissipates the least energy through ohmic losses at most pressures. Hydrogen has the least inductive energy storage at all pressures and greatest ohmic losses above 60 mTorr. Xenon presents the largest ohmic losses over the 10–60 mTorr range.

1. INTRODUCTION

Pulsed inductive plasma (PIP) devices have garnered much attention in recent years in the fusion [**? ? ? ? ?**] and spacecraft [**? ? ?**] communities. Of primary interest to the fusion community is deuterium, while the propulsion groups investigate heavier gases such as argon and xenon. However, the initial energy conversion process presents a substantial knowledge gap. Capacitors initially store energy which is then pulsed through strategically arranged inductive coils generating large currents that induce strong magnetic fields and opposing plasma currents. During a discharge, energy is divided between capacitive and inductive loads with energy being deposited into the plasma through mutual inductance coupling with the theta-pinch coil. Joule heating of the experiment and plasma losses (radiation, joule heating, wall transport, etc.) eventually dissipate all energy from the system. Of primary interest to both communities is understanding and controlling the energy coupling of the external circuit with the plasma.

This paper compares discharge current profiles of a cylindrical theta-pinch device with SPICE simulations to elucidate the temporal evolution of the energy coupling and losses associated with the gases of primary interest to the fusion and spacecraft communities over an applicable pressure range of 10–100 mTorr. Resulting plasma inductance and resistance values can be used to determine optimum operating pressures or gas species. Future studies can then explore the benefits of external circuit parameters, preionization voltage and position, gas injection, and charge voltage.

Section 2 of this paper details the experimental setup and test parameters. The circuit model used in this paper is presented in Sec. 3. Experimental results are presented in Sec. 4 with detailed simulation results and energy analysis discussed in Sec. 5. Final conclusions are presented in Sec. 6.

2. EXPERIMENTAL SETUP

To study the energy mechanisms associated with heavy-gas PIP devices, a series of tests were conducted using argon, hydrogen, and xenon gases at different fill pressures. Vacuum and fill pressures from 10–100 mTorr are presented. This section details the experiment setup and diagnostics used to obtain the data presented in this paper.

2.1. MISSOURI PLASMOID EXPERIMENT

The Missouri Plasmoid Experiment (MPX) Mk. II is a pulsed inductive test article located at the Aerospace Plasma Laboratory at Missouri S&T. MPX consists of a high-voltage capacitor and a single-turn eleven-segment theta-pinch coil. Each segment of the theta-pinch coil is constructed from aluminum 7075 and consists of two identical segment halves which are bolted together during assembly using two 0.95 cm diameter threaded rods. The resulting coil segment has a diameter measuring 17.8 cm and a thickness of 6.67 cm. The eleven segments are mounted horizontally and connected with four 1.27 cm diameter threaded rods. Nylon spacers machined to a 5.0 mm thickness are inserted between coil segments to allow for radial relief of magnetic diagnostics. The total length of the assembled theta-pinch coil is 78.35 cm. Aluminum plates measuring 78.35 cm × 12.7 cm × 0.64 cm are bolted to the theta-pinch coil to provide an interface for integrating the remaining MPX components. Four bolts per coil segment are used to attach the aluminum plates to the theta-pinch coil to reduce joint resistance and inductance.

A grade 214 quartz tube insulator is placed inside the theta-pinch coil and serves as the vacuum vessel for plasma formation. The quartz tube has an inner diameter of 15.5 cm and outer diameter of 16.1 cm and a length of 90 cm. Acrylic plates are located at both ends of the theta-pinch coil to ensure the quartz tube remains center aligned within the theta-pinch coil. The south end of the quartz tube is mated to the Missouri S&T vacuum facility [**?**] with a Duniway VBJG-7 L-gasket. An aluminum flange is mated to the north

end of the quartz tube using an identical L-gasket. Gas inlet and pressure gauge ports are located on the north flange. A MKS model 626 Baratron pressure gauge measures fill pressures of 0.01–100 mTorr.

A 0.707 μF capacitor is positioned approximately 20 cm from the edge of the theta-pinch coil. The Maxwell 33934 capacitor is rated for 70 kV and has a series inductance of 50 nH. A Excelitas GP-12B spark gap and TR-1700 trigger transformer are used to initiate the discharge of MPX. The adjacent electrode of the spark gap is connected to the anode of the capacitor and the opposite electrode is connected to the theta-pinch coil using a copper busbar. A second copper busbar is used to connect the capacitor cathode to the theta-pinch coil and passes through the center of a Pearson 4418 current monitor to measure discharge current. An acrylic insert is press-fit into the center of the current monitor to provide high voltage insulation and ensure the current monitor remains centered about the capacitor cathode. A tungsten electrode is inserted on the south flange and connected to a high voltage supply. This pre-ionization (PI) stage is set to 1.7 kV and provides seed electrons to assist the breakdown process. The MPX theta pinch coil and fully integrated system are shown in Fig. 2.1. More information regarding the triggering system and MPX diagnostics can be found in Refs. [**? ?**].
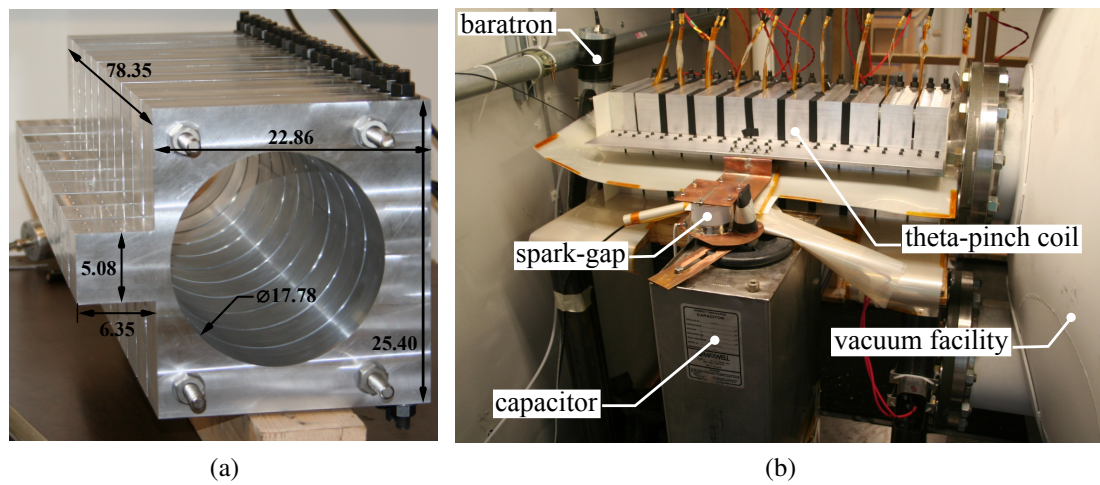
Figure 2.1. (a) Missouri Plasmoid Experiment (MPX) Mk. II theta pinch coil (units in cm) and (b) fully integrated MPX experiment attached to Missouri S&T Aerospace Plasma Laboratory vacuum facility.

3. CIRCUIT MODEL

This section presents the circuit model used to determine the partitioning of the MPX discharge energy. The determination of the MPX circuit parameters are discussed as well as the methodology for determining the equivalent circuit values for the plasma.

3.1. CIRCUIT DIAGRAM

A common circuit representation of a pulsed inductive device is illustrated in Fig. 3.1a [? ? ? ?] with an equivalent circuit given in Fig. 3.1b [? ?] to simplify analysis with SPICE. Unlike previous models [? ?], the primary and secondary inductances (L_p and L_s) are not

(a)

(b)
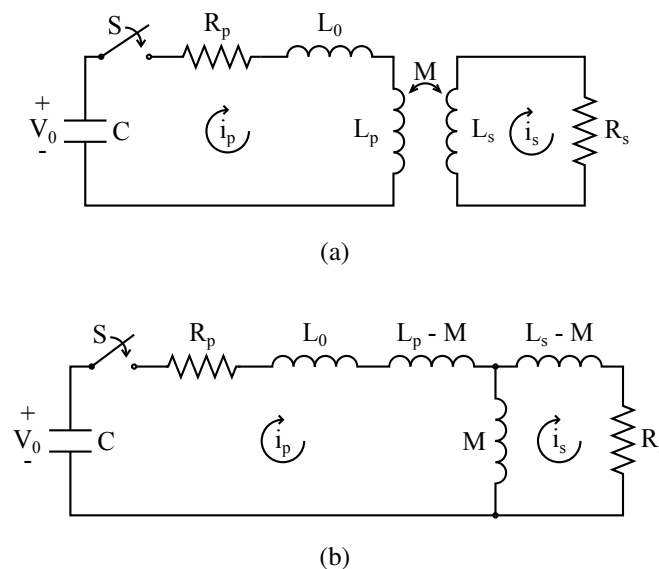
Figure 3.1. (a) Circuit model of a pulsed inductive device. (b) Equivalent circuit replacing inductors with a T network (Refs. [? ?])

assumed equivalent due to the cylindrical geometry of MPX and the presence of a quartz

tube insulator. The primary inductance is calculated using Eq. (9) in [**?**] yielding 36.2 nH. A few assumptions are made to calculate the mutual inductance:

1. plasma is a single-turn solenoid (N_2=1)

2. plasma and theta-pinch coil are equal length

3. plasma radius is same as quartz tube inner radius

4. plasma thickness is small

Mutual inductance of coaxial solenoids of equal length can then be solved using Eq. (36) in [**?**] giving a mutual inductance of 27.4 nH. Unlike [**? ? ? ? ?**], the plasma is not axially translated away from the device therefore no z dependence is considered in this model. Additionally, all circuit parameters are assumed constant over the discharge period and no radial compression of the plasma is assumed.

3.2. SIMULATION METHODOLOGY

The primary circuit parameters are found using vacuum test results and assuming a simple series RLC circuit model. Values of R, L, and C are iterated and the resulting current is compared to the MPX discharge current. Using a least squares estimate (LSE), the values of R, L, and C best approximating the vacuum discharge are 40.5 mΩ, 183.2 nH, 0.707 μF, respectively. Parasitic inductance L_0 is calculated by subtracting the primary inductance from the series inductance solution giving 147.0 nH. These values are used for all subsequent plasma simulations to calculate plasma resistance and inductance.

The plasma resistance and inductance (R_s and L_s) are solved using SPICE [**?**] simulations. A script is written in Python that iterates R_s and L_s values. For a given combination of circuit values, the script produces the necessary netlist and runs SPICE through batch command. The SPICE simulation returns the primary and secondary currents shown

in Fig. 3.1b and the primary current is then compared to the first 30 μs of the MPX discharge using a LSE. The combination of secondary circuit elements yielding the least error are presented as the effective plasma resistance and inductance.

4. EXPERIMENTAL RESULTS

This section presents the data from the single diagnostic used in this paper. MPX discharge current results are presented in both time and frequency domain. Data results from typical vacuum and plasma shots are presented. Vacuum tests are conducted at a pressure of 0.01 mTorr while plasma shots have prefills of argon, xenon, or hydrogen ranging from 10–100 mTorr and result in the formation of a plasma.

The Pearson 4418 current monitor measures the time-varying discharge current of MPX and all tests had an initial voltage of $15.0 \text{ kV} \pm 0.3\%$. In the vacuum case, a maximum current of 26.7 kA is measured. Plasma tests yield higher peak currents with a maximum of 27.5 kA observed for all three gas species. Fast-Fourier transform (FFT) and short-time Fourier transform (STFT) using MATLAB's built-in spectrogram function are used to analyze the current profile in frequency domain. FFT results show primary discharge frequencies of 442.6 and 465.4 kHz for the vacuum and plasma cases, respectively. For the STFT, a window length of 257 data points (14.3% of record length) with 95% overlap is used with a sampling frequency of 60 MHz and 2^{16} frequency points. The resulting spectrograms for the vacuum and plasma cases are presented in Figs. 4.1c and 4.1d, respectively. The STFT requires a full time window of data (4.29 μs in this case) before the frequency spectrum can be calculated. Because no waveform data are available before $t = 0$, the frequency spectrum for the first half-window cannot be determined and the spectrograms in Figs. 4.1c and 4.1d necessarily start at $t = 2.14 \ \mu$s. The spectrograms indicates that the initial frequencies of vacuum and plasma discharges were 441.8 ± 1.8 kHz and 463.3 ± 2.5 kHz, respectively. Plasma tests see the primary discharge current decrease at an earlier time than what is observed in vacuum tests.

The 5.3% increase in discharge frequency observed in Fig. 4.1b is combined with an increased dampening ratio resulting in a reduced number of current oscillations before returning to a quiescent state. Rather than having a single discharge frequency, a clear
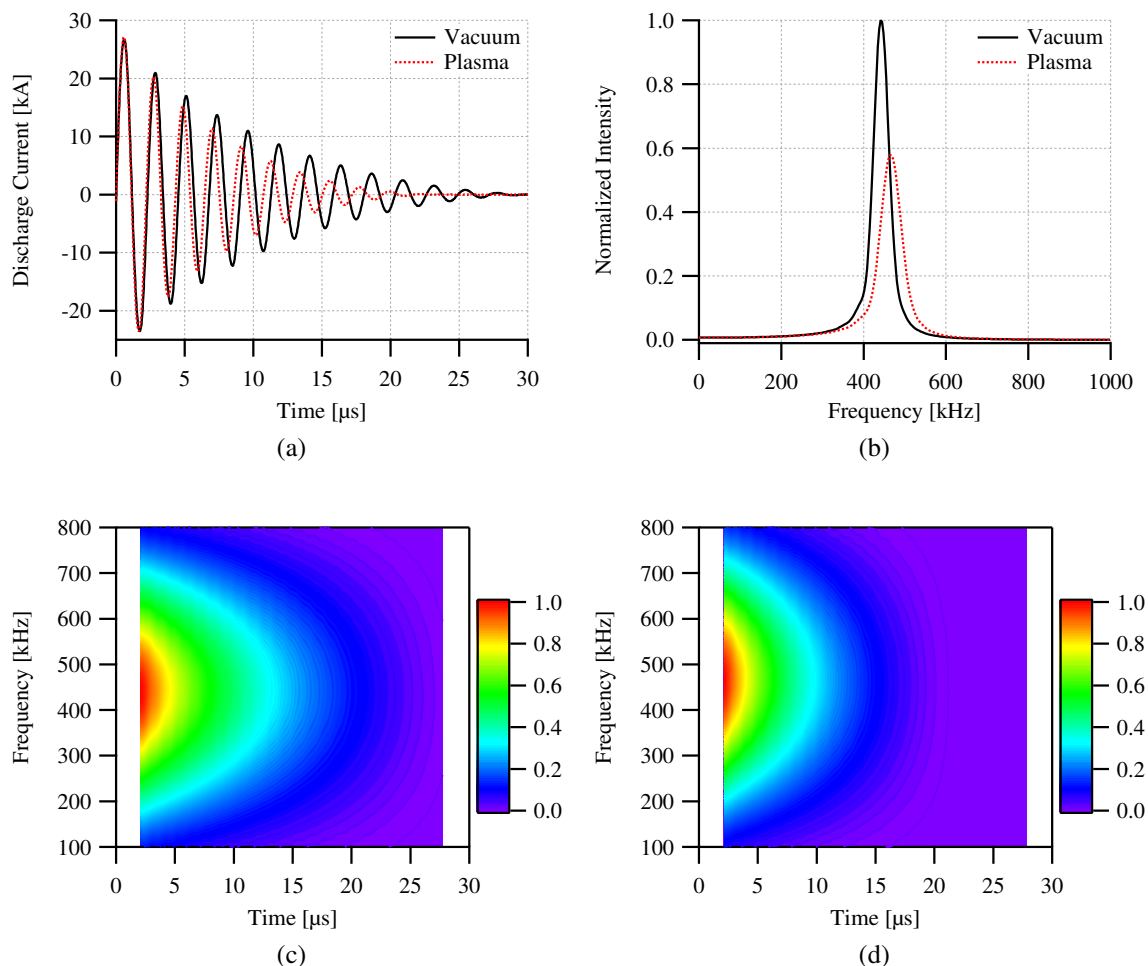
Figure 4.1. MPX discharge current measured with Pearson 4418 current monitor. Vacuum and plasma discharges are presented with time domain results in (a) and frequency domain results in (b-d). (b) Fast-Fourier transform of the full discharge, (c) spectrogram of vacuum test, and (d) spectrogram of typical plasma discharge. Illustrated plasma case taken with a 10 mTorr argon prefill.

broadening in the frequency domain is observed in both the vacuum and plasma cases. When plasma is present, the peak intensity of the FFT is reduced to 57.8% of the vacuum peak intensity and has a full-width half-max of 61.1 kHz compared to 44.9 kHz for the vacuum case, an increase of 36.1%.

5. DISCUSSION

Argon, hydrogen, and xenon gases are tested from 10–100 mTorr in 10 mTorr increments with each test condition repeated five times. The experimental discharge currents have a variation of $\pm 2\%$. Values of R_s and L_s are simulated to a resolution of 0.1 mΩ (0.4%) and 0.1 nH (0.2%), respectively.

5.1. CURRENT COMPARISON

Examples of vacuum and plasma simulation currents are plotted against MPX primary discharge current in Fig. 5.1. By assuming time-invariant circuit parameters, the simulation does not match the primary discharge current exactly. The simulation over-predicts the peak discharge current magnitude by $3.7 \pm 0.2\%$ on the vacuum tests and an average of $5.0 \pm 0.6\%$ on plasma tests. The largest error in current magnitudes observed in the first 60% of the discharge occurs at approximately 40% of the full discharge time. The full discharge time is defined as the time required for the current to return to a quiescent state. For the vacuum and plasma tests, the full discharge times are 30.0 and 22.7 μs, respectively. For vacuum, the maximum error is 8.4% at 11.9 μs and 8.5% at 9.2 μs for a 80 mTorr argon plasma. Between 40–60% of the full discharge time, the deviation between simulation and experimental current magnitude decreases. In the last 40% of the discharge, the primary circuit resistance R_p increases rapidly as the spark gap switch opens, further reducing agreement. However, 98.6% of the initial energy has been dissipated through ohmic losses in the first 60% of the discharge. The poor model agreement during the last 40% of the discharge therefore has negligible impact on the results presented in this paper. Using a FFT, the center frequency of the MPX discharge can be compared to the resonant frequency of the simulation solution. The vacuum tests presented 442.6 kHz center discharge frequency compared to 441.3 kHz in simulations, a difference of 0.3%. Plasma tests agree with simulation with an average difference of 0.8%. All three gases show best frequency
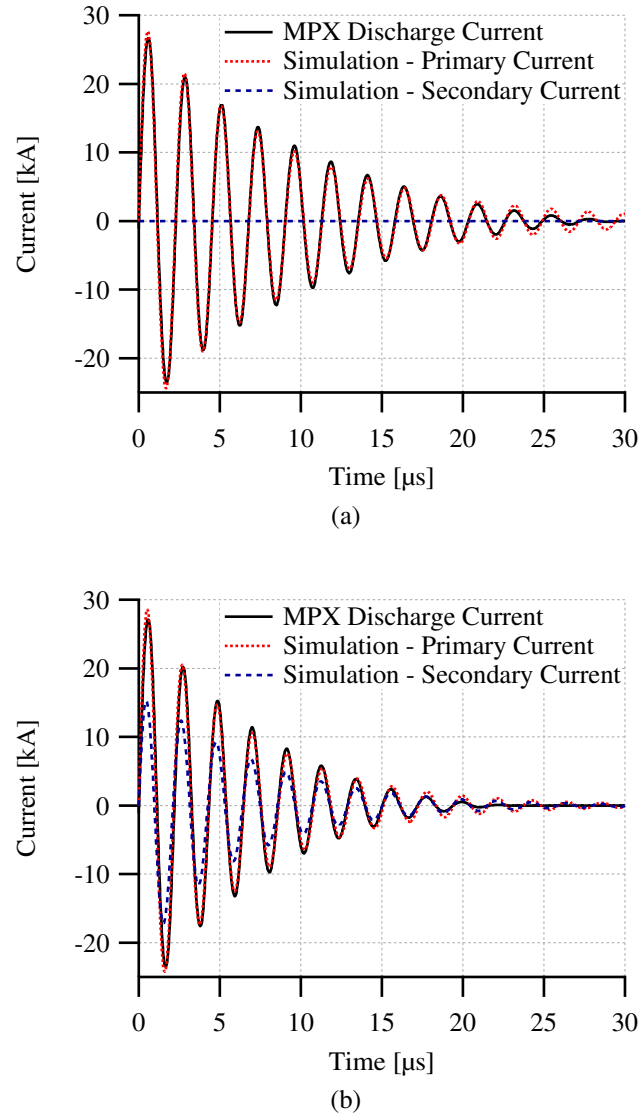
Figure 5.1. Comparison of (a) vacuum and (b) plasma simulation currents with measured MPX discharge current. Illustrated plasma case taken with a 10 mTorr prefill of argon.

agreement at 30 mTorr. Hydrogen produced the best frequency agreement with an average simulated frequency of 460.4 kHz$\pm$0.3% compared to a average MPX discharge frequency of 463.7 kHz$\pm$0.3%, a difference of 0.7%. No direct methods of measuring plasma current were implemented during testing therefore errors relative to the simulated secondary current could not be quantified.

5.2. SIMULATION RESULTS

The circuit parameters calculated from the LSE SPICE analysis are plotted as functions of pressure in Fig. 5.2. Plasma resistance is due to the collisionality of the plasma. For
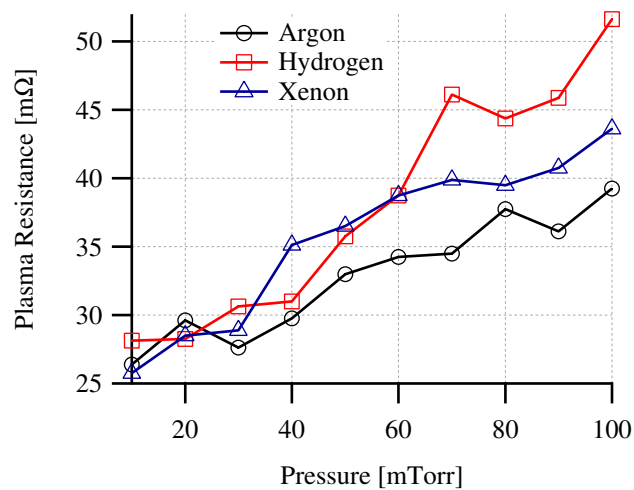
(a)
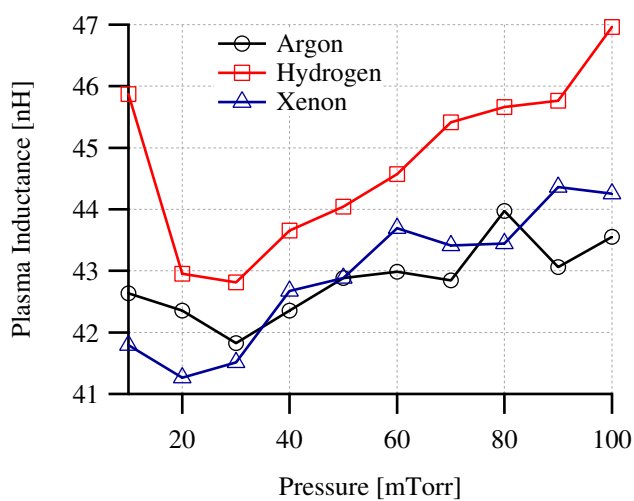
(b)

Figure 5.2. Resulting plasma (a) resistance and (b) inductance from LSE analysis of circuit simulations and MPX discharges from 10–100 mTorr.

all three gases, the plasma resistance is found to vary between 25.8 and 51.8 mΩ. These

results agree with the 10–100 mΩ [?] estimate presented in literature. Over the pressure range tested, the resistance of argon, hydrogen, and xenon increased by 56.7%, 94.2%, and 77.0%, respectively. Assuming a long annular cylinder of plasma with a thickness of 5 mm (from [?]), the resistivity for the 10 and 100 mTorr argon prefills are 214 and 429 Ω-μm, respectively, in agreement with the literature. [? ?] The pressure dependence of the xenon resistance closely matches that of argon but averages 4.0 mΩ (12.5%) higher from 40–100 mTorr. The resistance of hydrogen is comparable to argon and xenon from 10–40 mTorr, but increases faster than the other gases after 40 mTorr.

The inductance of all three species varies from 41.3–47.0 nH. Inductance is minimized at 30 mTorr for argon and hydrogen while xenon is minimized at 20 mTorr. From 30–50 mTorr, the inductance of xenon closely matches that of argon, varying by an average of 0.5%. After 50 mTorr, the inductance of argon and xenon deviate with xenon averaging a 0.8 nH (1.9%) increase over argon with the exception of 80 mTorr when argon inductance exceeds xenon by 0.5 nH (1.2%). The inductance of hydrogen is largest of the three species tested with an average increase of 1.1 nH (2.6%) from 20–60 mTorr and 2.6 nH (6.0%) from 70–100 mTorr, relative to argon. After 60 mTorr, the pressure dependence on hydrogen inductance increases 284% and 147% faster than argon and xenon, respectively, and xenon increases 55% faster than argon.

5.3. ENERGY ANALYSIS

During the MPX discharge ($t > 0$), the energy initially stored in the capacitor is distributed between capacitive and inductive elements in the primary and secondary circuits or dissipated through resistance as shown in Eq. (5.1)

$$
\begin{aligned}
\tfrac{1}{2}CV_0^2 &= \tfrac{1}{2}CV_p^2(t) + \int_0^t I_p^2(\tau)R_p d\tau + \int_0^t I_s^2(\tau)R_s d\tau \\
&\quad + \tfrac{1}{2}L_0 I_p^2(t) + \tfrac{1}{2}L_p I_p^2(t) - I_p I_s M + \tfrac{1}{2}L_s I_s^2(t).
\end{aligned}
\tag{5.1}
$$

Using the results from the circuit simulations, the temporal evolution of the energy partitioning can be calculated. The results of a 10 mTorr argon prefill are shown in Fig. 5.3b.
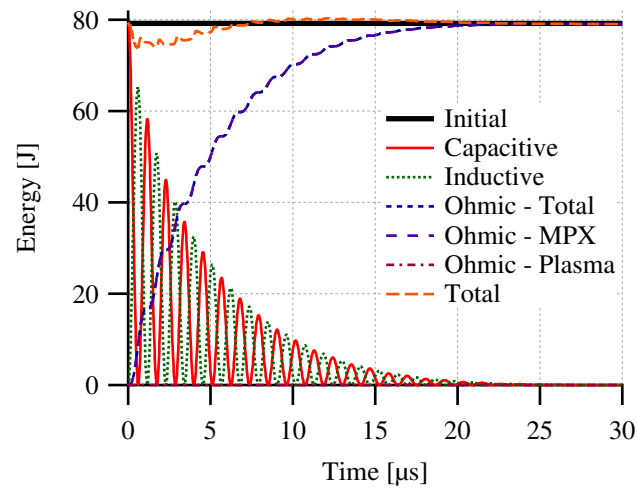
(a)
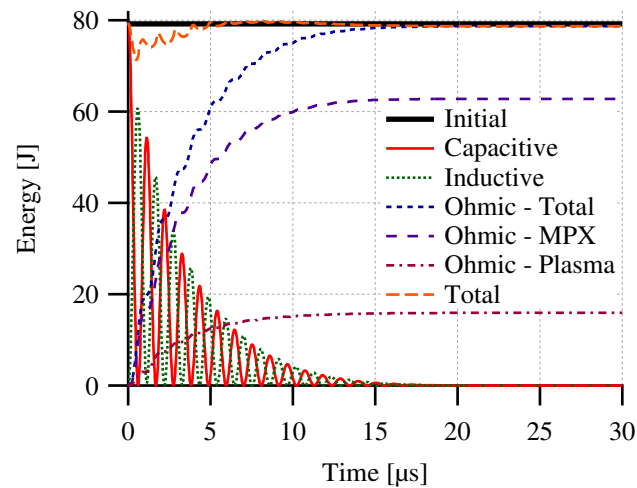
(b)

Figure 5.3. Temporal evolution of energy partitioning in capacitive, inductive, and ohmic loads for (a) vacuum and (b) plasma tests. Illustrated plasma case taken with a 10 mTorr prefill of argon.

The inductive energy plotted is the summation of the energies stored in all four inductive loads. The ohmic energy is split into the contribution from the MPX circuit and the plasma; in the case of a 10 mTorr argon prefill (Fig. 5.3b), 15.9 J (20.1%) of the initial energy is dissipated by the plasma.

Variation between the experimental and theoretical currents shown in Fig. 5.1b result in total energies that drop below the initial 79.2 J stored in the capacitor. This is a result of attempting to fit constant value circuit parameters to a dynamic system. The plasma parameters produced from the LSE analysis combined with the simulated currents produce a total energy that exactly equals the initial energy at all times. However, simulated primary currents over predict the experimental currents at early times resulting in a small deficit in the total energy relative to the initial energy. For vacuum tests, the maximum deficit was $6.9 \pm 0.3\%$ of the initial energy compared to $9.2 \pm 0.9\%$ for plasma tests. At later times, 5.1 μs for vacuum and 3.77 μs for plasma tests, the simulated primary current under predicts the experimental current resulting in a total energy that exceeds the initial energy. The simulated current starts to over predict current at later times, 18.6 μs for vacuum and 13.4 μs for plasma tests, but by this point over 98% of the initial energy has been ohmically dissipated regardless of which current is considered. The simulated current dissipates an additional 0.12 J (0.16%) of the initial energy relative to the experimental current for a given solution of plasma circuit parameters. An increase in total energy deficit is observed for plasma tests because the plasma current is directly proportional to the primary circuit current. Therefore the over prediction of the simulation current has a compounding effect.

The inductor models the energy stored within plasma and the resistance models the energy dissipated by the plasma and other loss mechanisms. These two contributions are shown in Figs. 5.4 and 5.5, respectively.

Inductive energy for argon is presented in Fig. 5.4a at select pressures. The resulting maximum energy for all gases and pressures are plotted in Fig. 5.4b. All three gases show maximum inductively stored energy occurs at time 1.6 μs at 30, 20, and 10 mTorr for
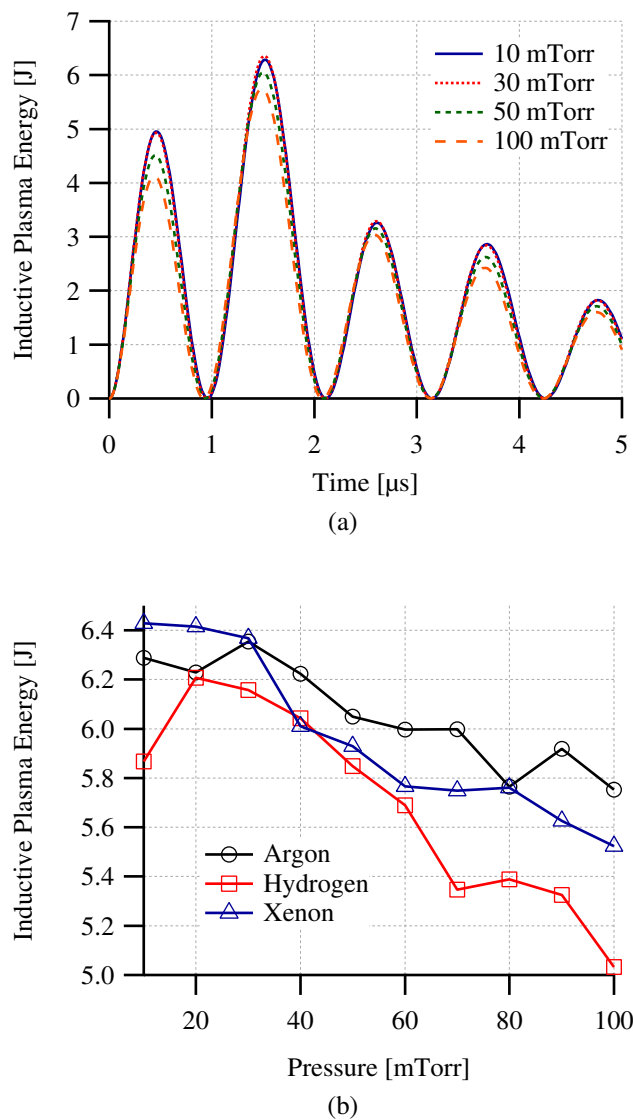
Figure 5.4. (a) Temporal evolution of plasma inductive energy and (b) maximum inductive energy stored in plasma as a function of gas species and prefill pressure.

argon, hydrogen, and xenon, respectively. The temporal evolution of the energy dissipated through ohmic heating is presented for select prefill pressures of argon in Fig. 5.5a and for all gas species and pressures in Fig. 5.5b. All three species show increased ohmic energy dissipation as pressure increases. At 100 mTorr 25.3%, 26.7%, and 26.3% of the initially stored energy is dissipated by argon, hydrogen, and xenon, respectively.
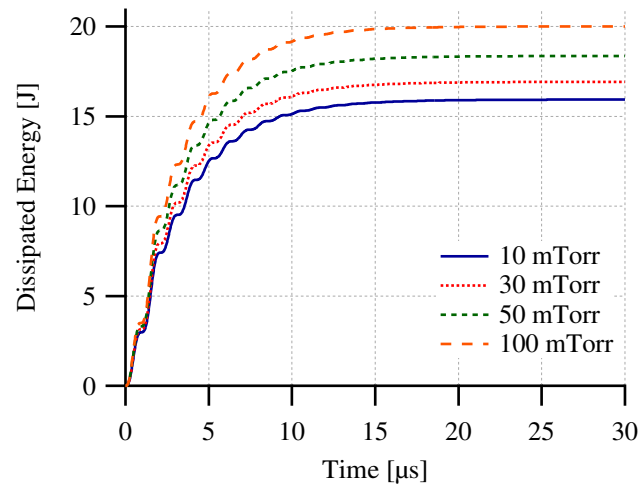
(a)
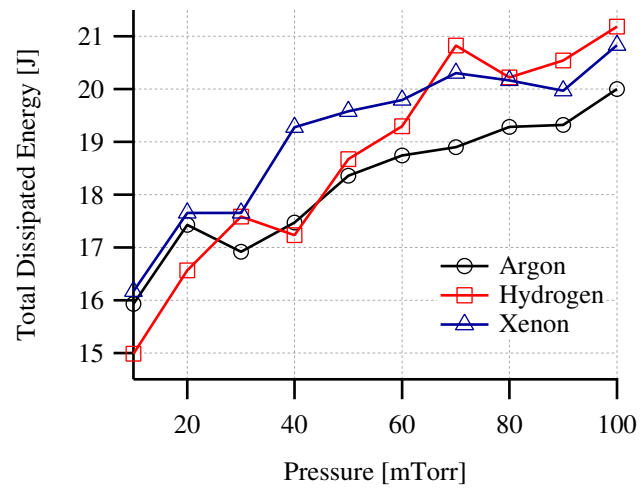
(b)

Figure 5.5. (a) Temporal evolution of energy resistively dissipated by plasma and (b) total dissipated energy as a function of gas species and prefill pressure.

6. CONCLUSIONS

A simple method of estimating inductively coupled plasma parameters using SPICE has been presented. Simulations indicate that inductive energy deposited into the plasma initially increases with pressure to a local maximum for argon and hydrogen and then decrease significantly with increasing prefill pressure. Test with xenon suggests that the maximum deposited inductive energy occurs with a prefill pressure between zero and 10 mTorr. For all three gases, simulations show increased energy ohmically dissipated by the plasma as prefill pressure is increased. The presence of a local maximum in inductively coupled plasma energy suggests a potential optimum design condition may exist for each gas species depending on intended application. For example, experiments where plasma compression is used to generate fusion may observe the greatest performance with a 20 mTorr hydrogen prefill and a compression timing of 1.6 μs as this would maximize the amount of energy in the plasma.

Simulated properties have shown to be in agreement with established literature with plasma resistivity varying between 214 and 429 Ω-μm. Temporal evolution of the plasma indicates that 8.1% or less of the initial energy is inductively stored in the plasma while 15.0–21.2 J (18.8–26.7%) of the initial energy is dissipated through plasma ohmic losses. Inductive energies are maximized at three quarters of the first discharge cycle when current is most negative. More inductively coupled energy is stored in argon for pressures of 30 mTorr and above while xenon averages 2.2% more energy than argon and 6.5% more than hydrogen from 10–20 mTorr. Hydrogen yields the largest plasma inductance over the tested pressure range.

ACKNOWLEDGMENTS

III. EFFECTS OF DC PREIONIZATION VOLTAGE AND RADIAL LOCATION ON PULSED INDUCTIVE PLASMA FORMATION

Ryan A. Pahl and Joshua L. Rovey

Missouri University of Science and Technology, Rolla, Missouri, 65401, USA

ABSTRACT

The effects of DC preionization voltage and radial location on plasma formation repeatability are presented for argon prefills of 20–200 mTorr with a discharge energy of 79.5 J at 15 kV. Current profiles of a ringing theta-pinch are compared to circuit simulation in SPICE to estimate plasma resistance and inductance and quantify plasma formation uncertainty. Plasma thickness is calculated using axial imaging and experiment geometry and used to determine the mutual inductance coupling of the plasma and the theta-pinch coil. At all pressures tested, plasma formation failed to occur in the absence of DC preionization. At pressures less than 100 mTorr, preionization voltage has a significant impact on plasma formation, repeatability, and energy coupling into the plasma. At 20 mTorr, 0.20 W of DC power is sufficient to stabilize plasma formation at the first zero-crossing of the current. With 1.5 W an additional 39% of inductive energy is coupled into the plasma. Increasing pressure also increased plasma repeatability and resulted in a convergence of plasma circuit parameters.

1. INTRODUCTION

Pulsed inductive plasma (PIP) devices have garnered much attention in recent years in the fusion [**? ? ? ? ?**] and spacecraft [**? ? ?**] communities. Of primary interest to the fusion community is deuterium, while the propulsion groups investigate heavier gases such as argon and xenon. However, the initial energy conversion process presents a substantial knowledge gap. Capacitors initially store energy which is then pulsed through strategically arranged inductive coils generating large currents that induce strong magnetic fields and opposing plasma currents. During a discharge, energy is divided between capacitive and inductive loads with energy being deposited into the plasma through mutual inductance coupling with the theta-pinch coil. Joule heating of the experiment and plasma losses (radiation, joule heating, wall transport, etc.) eventually dissipate all energy from the system. Of primary interest to both communities is understanding and controlling the energy coupling of the external circuit with the plasma.

This paper investigates the effects of DC preionization (PI) source location and voltage on argon plasma formation over a pressure range of 20–200 mTorr. SPICE simulations are used to analyze experiment discharge current profiles and determine equivalent circuit parameters of the plasma. Improvements over previous work [**?**] are achieved with photomultiplier tubes which allow for a subset of the discharge current corresponding to plasma presence to be used in the SPICE model. Furthermore, plasma thickness is determined from axial imaging which is then used to calculate the mutual inductance between the plasma and theta-pinch coil.

Section 2 of this paper details the experimental setup and test parameters. The circuit model used in this paper is presented in Sec. 3. Experimental results are presented in Sec. 4 with detailed simulation results discussed in Sec. 5. Final conclusions are presented in Sec. 6.

2. EXPERIMENTAL SETUP

To analyze the effects of a DC PI source on pulsed inductive plasma formation, a series of experiments were conducted. The tests were performed using the Missouri Plasmoid Experiment (MPX Mk. II) and Missouri S&T Space and High-Altitude Environment Testing Facility (Fig. 2.1) with argon prefills ranging from 20–200 mTorr. More detailed information on the MPX Mk. II geometry, discharge characteristics, and diagnostics can be found in Refs. [?] and [?].
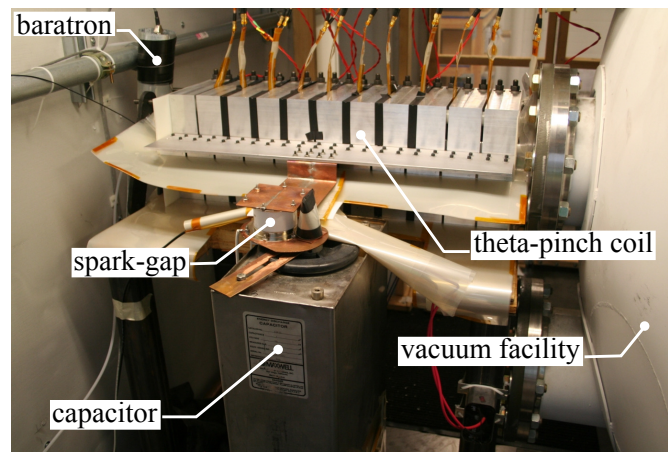
Figure 2.1. Missouri Plasmoid Experiment (MPX) Mk. II attached to Space and High-Altitude Environment Testing Facility in the Missouri S&T Aerospace Plasma Laboratory.

Two DC PI sources were placed at experiment radii corresponding to $r = 0.0R$ and $r = 0.8R$, where R is the radius of the quartz tube. The DC sources are driven by a Matsusada RB10-10P power supply with a maximum output of 1 mA at 10 kV. Five DC voltages are used for each probe at each pressure tested. The voltage range is bracketed by the lowest stable output of the preionization circuit (400 V) and the breakdown voltage of the prefill gas. Once the upper and lower bounds were determined, the voltage range

was divided evenly into fifths. The resulting upper and lower bounds of the voltage range

associated with each prefill pressure are tabulated in Table 2.1. Both the 100 and 200 mTorr

Table 2.1. Voltage and current of DC preionization source at the lowest and highest voltage settings. Reported error is one standard deviation of the measured value.

Pressure [mTorr]	Setting 1		Setting 5	
	Voltage [V]	Current [mA]	Voltage [V]	Current [mA]
20	$398 \pm 0.6\%$	$(10.8 \pm 1.9\%)$	$1498 \pm 0.4\%$	$(998 \pm 2.7\%)$
40	$417 \pm 8.9\%$	$(10.9 \pm 2.7\%)$	$800 \pm 0.1\%$	$(942 \pm 3.3\%)$
60	$401 \pm 0.4\%$	$(10.8 \pm 0.0\%)$	$599 \pm 0.2\%$	$(745 \pm 1.7\%)$
80	$400 \pm 0.0\%$	$(10.8 \pm 0.0\%)$	$559 \pm 0.2\%$	$(845 \pm 1.1\%)$
100	$399 \pm 0.3\%$	$(10.8 \pm 0.0\%)$	$556 \pm 0.3\%$	$(1117 \pm 0.1\%)$
150	$399 \pm 0.2\%$	$(10.8 \pm 0.0\%)$	$589 \pm 0.3\%$	$(83.8 \pm 5.6\%)$
200	$401 \pm 0.2\%$	$(10.8 \pm 0.0\%)$	$567 \pm 0.3\%$	$(179 \pm 3.5\%)$

pressures presented a challenge at the highest voltage. The initial target for these two

pressures was 600 V and thus 50 V increments. However, during testing the highest value

that could be consistently achieved without breaking down the gas was less than 600 V. For

these two pressures, the voltage increment is 50 V even though the 600 V upper limit was

not achieved.

3. CIRCUIT MODEL

This section presents the SPICE circuit model used to elucidate equivalent plasma circuit parameters. The determination of the MPX circuit parameters are discussed as well as the methodology for determining mutual inductance and the equivalent circuit values for the plasma.

3.1. CIRCUIT DIAGRAM

A common circuit representation of a pulsed inductive device coupled to a plasma through a mutual inductance is illustrated in Fig. 2(b) of Ref [?]. Unlike previous models [? ?], the primary and secondary inductances (L_p and L_s) are not assumed equivalent due to the cylindrical geometry of MPX and the presence of a quartz tube insulator which provides a stand-off from the wall of the inductor. The inductance of the theta-pinch coil (primary inductance) is calculated using Eq. (9) in [?] yielding 36.2 nH. A few assumptions are made to calculate the mutual inductance:

1. plasma is a single-turn solenoid ($N_2=1$)

2. plasma and theta-pinch coil are equal length

3. plasma outer radius is same as quartz tube inner radius

The mutual inductance of coaxial solenoids of equal length can then be solved using Eq. (36) in Ref. [?] once plasma thickness is known. This is determined using axial imaging with a Canon EOS Rebel XT with a focal length of 50 mm, a f-stop of 10, an ISO of 100, and an exposure length of 1 second. Plasma images are processed with the Python PIL library to determine the plasma geometry. This process in discussed in greater detail in Sec. 4.2.

3.2. SIMULATION METHODOLOGY

To determine equivalent circuit parameters of the plasma, SPICE simulations are used for a given R_s and L_s. The resulting primary circuit current is compared to MPX discharge currents and the Nelder-Mead simplex [?] method is used to minimize the error function in a least-squares sense to determine R_s and L_s. To better approximate the plasma parameters, eight Ocean Optics 200 μm fiber optic patch cables were placed in the gaps between coil segments 2–10 looking in the $\hat{r}$ direction and connected to Hamamatsu HC120-05 photomultiplier tubes (PMTs) to determine the time interval for which plasma is present. The SPICE simulation fits only the discharge current in this time interval. Python is used to produce the necessary SPICE netlist for the updated R_s and L_s from each iteration of the simplex method and call SPICE through batch command.

Primary circuit values were found using vacuum test results and a simplified series RLC model. The values of R, L, and C best approximating the vacuum discharge are 40.4 mΩ, 185.1 nH, 707 nF, respectively. Parasitic inductance L_0 is calculated by subtracting the primary inductance (theta-pinch coil) from the series inductance solution giving 148.8 nH.

4. EXPERIMENTAL RESULTS

This section presents a subset of the data collected from the various diagnostics used in this paper. Argon prefill pressure is varied from 0–100 mTorr in 20 mTorr increments and then in 50 mTorr increments from 100–200 mTorr. Discharge current for a typical MPX shot is presented in Fig. 4.1 along with the resulting PMT signals. Due to axial variations in plasma formation, the 8 PMT signals are summed to give a global plasma initiation time.

4.1. DISCHARGE CURRENT
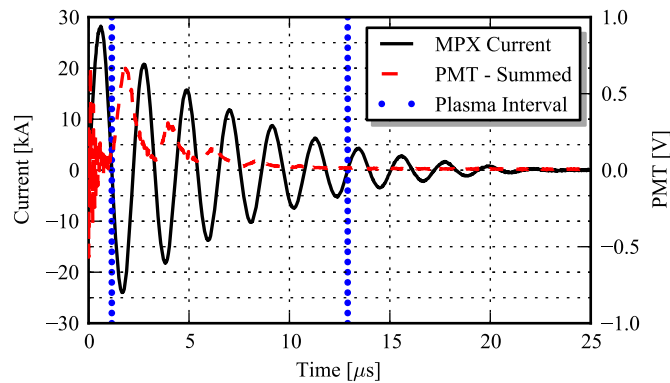
Figure 4.1. Discharge current and summation of all 8 PMT outputs for test 1405160015. 20 mTorr argon discharge with a DC preionization voltage of 1500 V at 980 μA.

It is apparent in Fig. 4.1 that plasma formation occurs at the first zero-crossing (1.2 μs) of the discharge current and has fully decayed by 12.9 μs. The SPICE model discussed in Sec. 3.2 attempts to fit the discharge current in this time interval. For 20 mTorr prefills, the lowest two PI voltages resulted in significant fluctuations in plasma formation time with breakdown occurring between the second and fifth zero-crosses of the discharge current. At higher PI voltage the plasma breakdown time became more repeatable and

always occurred at the first zero-cross. Higher pressures showed greater repeatability over the full range of PI voltages. Prefill pressures of 60, 80, and 100 mTorr had a single test start at the second zero-cross. This occurred at the lowest PI voltage for the 60 and 80 mTorr tests and at the second lowest voltage for the 100 mTorr test. At 150 mTorr, a single test showed plasma formation occurring at the beginning of the discharge. Plasma formation near magnetic field nulls is observed in literature and discussed in more detail in Refs. [?] and [?]. Discharge current profiles and plasma simulation currents are discussed in detail in Ref. [?].

4.2. PLASMA THICKNESS

Two image processing examples used to estimate average plasma thickness are shown in Fig. 4.2 illustrating the image mask for tests at 20 and 200 mTorr, the highest voltage settings, and at $r = 0.0R$. The plasma image is first converted to an 8-bit grayscale image with a pixel intensity varying from $0 \leq i \leq 255$. A transparent mask is generated from pixels with an intensity of $i \geq 165$ which identifies the region of plasma activity. Due to obstructions in the image due to probe cables and solenoid isolation valve (lower-right corner), only the top-half of the image mask is used to determine average plasma thickness. The ratio of pixels at or above the intensity threshold to the maximum possible number of pixels is proportional to the cross-sectional area of the plasma relative to the cross-sectional area of the quartz tube. Using the experiment geometry, the plasma thickness is then easily determined from trigonometry. At low pressures the plasma shape appears amorphous with aberrations becoming more pronounced at increased PI voltage. As pressure increases, the plasma takes on an annular shape.

Shot: 1405160015
Gas: Argon - 20.0 mTorr
PI Setting: 1500.0 V, 980.0 uA
PI Location: 0.0R
Delay: 0 s - ND: 0 - ISO: 100

(a)   (b)

Shot: 1405160285
Gas: Argon - 200.0 mTorr
PI Setting: 570.0 V, 189.4 uA
PI Location: 0.0R
Delay: 0 s - ND: 0 - ISO: 100

(c)   (d)
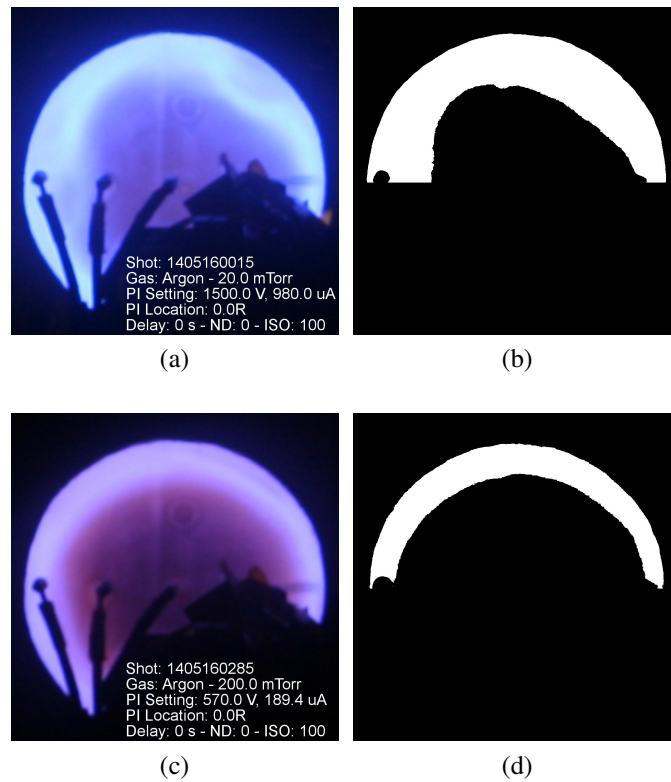
Figure 4.2. Original plasma images and masks for pixel intensities $i \geq 165$. 20 mTorr argon prefill is shown in (a) with corresponding mask in (b). Similarly, a 200 mTorr argon prefill is presented in (c) and (d).

5. DISCUSSION

Results of SPICE simulation are presented in this section. Plasma resistance and inductance circuit parameters are presented for only the lowest and highest values of PI voltages for a given pressure. The remaining PI voltages fall between the two extreme and offer no additional insight.

5.1. PLASMA THICKNESS

The plasma thickness for the highest and lowest PI voltages are presented in Fig. 5.1. For pressures less than 100 mTorr, plasma geometry is highly dependent on PI voltage.
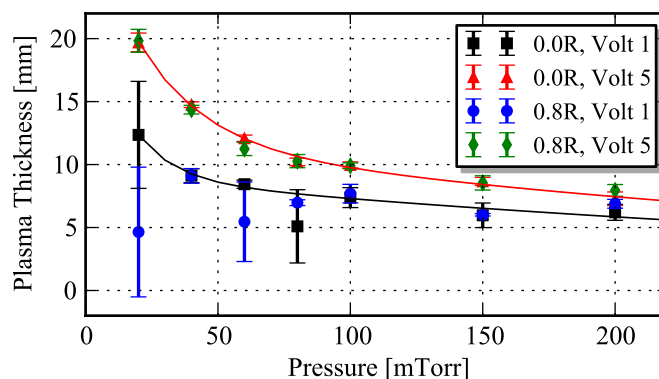
Figure 5.1. Plasma thickness of argon prefills from 20–200 mTorr for lowest and highest PI voltage.

Higher voltages consistently provided larger plasma volumes with a high degree of repeatability. At 20 mTorr, the highest PI voltage yielded plasma thicknesses of 19.7 ± 0.7 mm and 19.8 ± 0.8 mm for $r = 0.0$R and $r = 0.8$R, respectively, compared to 12.4 ± 4.2 mm and 4.6 ± 5.2 mm for the lowest PI voltage. As argon prefill pressure is increased, plasma formation becomes more repeatable and at 100 mTorr, plasma formation repeatability ap-

pears to be independent of PI voltage. As prefill pressure increases, the plasma thickness for the low and high PI voltages start to converge and plasma thickness dependence on PI voltage decreases with increased pressure. At 200 mTorr, the lowest PI voltage yielded average plasma thicknesses of 6.2 ± 0.6 mm and 6.9 ± 0.4 mm for $r = 0.0R$ and $r = 0.8R$, respectively, compared to 7.3 ± 0.5 mm and 7.9 ± 0.4 mm for the highest PI voltage. The $r = 0.0R$ data are easily modeled with a double exponential regression yielding $t_{\text{plasma}} = 11.91e^{-0.0024p} + 18.54e^{-0.0397p}$ mm for the highest PI voltage, where p is the prefill pressure measured in mTorr. Ignoring the outlier at 80 mTorr, the plasma thickness at the lowest PI voltage is modeled by $t_{\text{plasma}} = 9.071e^{-0.0022p} + 14.27e^{-0.0681p}$ mm.

From Rosa and Grover (Ref. [?]),

$$M \propto \langle r_{\text{plasma}} \rangle^2 = (1 - \langle t_{\text{plasma}} \rangle)^2,$$

therefore decreasing plasma thickness corresponds to larger average plasma ring radius and thus increased mutual inductance. Regression lines are fit to the mutual inductance as functions of pressure and are shown in Eq. (5.1). The experiment geometry limits the plasma mutual inductance to a maximum of 27.2 nH for an infinitely thin plasma at the wall of the quartz insulator; however, this was not observed in the pressure range tested.

$$M(p) = \begin{cases} 2.190\ln(620.4p) & : 20 \leq p \leq 80 \\ 8.361 \times 10^{-3}p + 22.95 & : 80 < p \leq 200 \end{cases} \tag{5.1}$$

5.2. SIMULATION RESULTS

The uncertainty of circuit parameters calculated from the SPICE analysis are plotted as functions of pressure in Figs. 5.2a and 5.2c. Plasma resistance and inductance uncertainty are calculated as the percentage of the standard deviation relative to the mean value and are given in Figs. 5.2a and 5.2c. Plasma energy terms are calculated using the

methods presented in Ref. [**?**]. Plasma total ohmic and peak inductive energies are presented in Figs. 5.2b and 5.2d. For all PI voltages and locations, plasma resistance increased
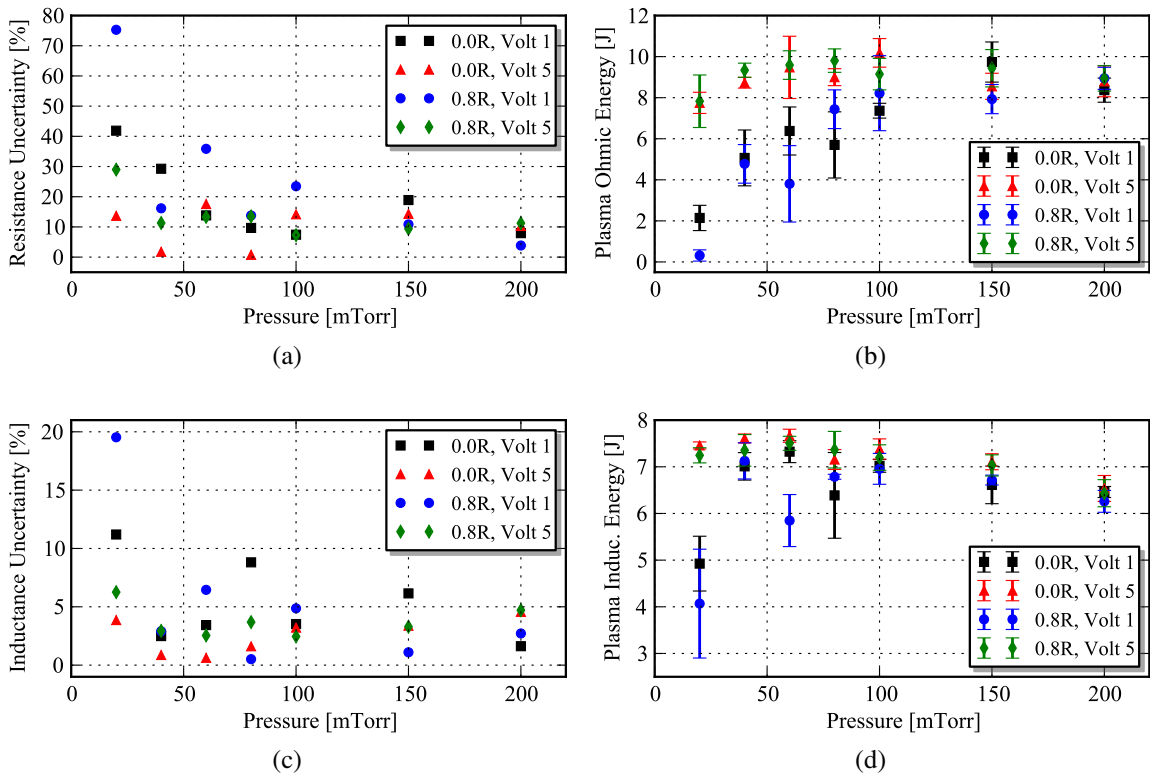
Figure 5.2. Results of SPICE simulation using Nelder-Mead Simplex method. (a) plasma resistance uncertainty, (b) plasma ohmic energy, (c) plasma inductance uncertainty, and (d) plasma inductive energy.

with argon fill pressure due to the increased collisionality of the plasma. The uncertainty of the plasma resistance is largest for low fill pressures and decreases with increased gas pressure. Plasma formation repeatability shows a significant dependence on PI voltage at low pressures and less dependence at pressures greater than 100 mTorr. For the $r = 0.0R$ location, plasma resistance increased 309% and 123% for the lowest and highest PI voltages, respectively, as fill pressure increased from 20–200 mTorr. Larger PI voltages yield increased plasma resistances from 20–100 mTorr at which point the resistance converges

with variations of 4–6% at 200 mTorr. This appears counter intuitive at first as one would expect hotter plasmas to have lower plasma resistances. However, the simulated resistance is analogous to the loss mechanisms of the plasma rather than a simple indication of plasma energy or temperature. Tests with high PI voltage dissipate larger plasma current than tests using lower PI voltages which induce significantly smaller plasma currents. At 20 mTorr, the highest PI voltage had a peak plasma current of 26.4 ± 0.7 kA while the lowest PI voltage produced 17.1 ± 3.5 kA. The peak plasma current for the largest PI voltages at $r = 0.0$R can be modeled by the logarithmic regression: $I_s = 46.74 - 2.899 \ln(48.08p)$ kA.

Plasma inductance shows a high degree of uncertainty at low PI voltages and low prefill pressures while the largest PI voltages exhibit a logarithmic dependence on prefill pressure with uncertainties remaining below 5% for all but $r = 0.8$R test at 20 mTorr. Plasma inductance increases an average of 61.8% for the largest PI voltage while the lowest PI voltage resulting in an average increase of only 22.4% from 20–200 mTorr. Fig. 5.2d shows plasma inductive energy is relatively unchanged from 20-100 mTorr for the highest PI voltage with an average value of 7.5 ± 2.7% J and 7.3 ± 1.6% J for the $r = 0.0$R and $r = 0.8$R locations, respectively. Lower PI voltages at low pressures result in poor energy coupling of the discharge circuit into the plasma. At 20 mTorr, 39% less energy is coupled into the plasma for the lowest PI voltage relative to the highest. However, by 100 mTorr, the inductive energy dependence on PI voltage is negligible.

6. CONCLUSIONS

Circuit parameter uncertainty for an inductively coupled argon plasma have been determined through SPICE simulations for a range of applicable pressures, DC preionization voltages, and locations. Plasma formation is sporadic for 20 mTorr prefills at the two lowest PI voltages but stabilizes as PI voltage or prefill pressure increases such that plasma initiation occurs at the first zero-crossing of the discharge current. At prefill pressures $\geq$ 100 mTorr, PI voltage was found to have minimal impact on discharge repeatability. Over the pressure range tested, varying PI location from the center of the quartz tube to near the wall had negligible effect on plasma geometry, repeatability, or equivalent circuit parameters. This suggests that location of the DC PI source is inconsequential, it is only critical that the PI is present. Tests also indicate minimal power is needed to insure repeatable plasma formation. 0.20 W of DC power is sufficient to stabilize plasma formation timing and 1.49 W provides repeatable plasma properties at 20 mTorr. For systems operating at higher pressures significantly less power is needed. At 200 mTorr, 4.3 mW is needed to produce repeatable plasma properties. Without PI voltage, plasma formation was not possible.

ACKNOWLEDGMENTS

SECTION

3. CONCLUSIONS

The main emphases of this dissertation are: construct a pulsed inductive test article, develop high accuracy magnetic probes, quantify the energy coupling of the discharge circuit into the inductively coupled plasma, and quantify the effects of DC preionization on plasma formation repeatability. The Missouri Plasmoid eXperiment was constructed to satisfy the first requirement and the two iterations of MPX have been presented and discussed. Three journal papers are presented to address the remaining elements of this dissertation. The first paper focused on the construction and calibration of a magnetic field probe. Two differential $\dot{B}$ probes were presented. A custom $\dot{B}$ probe is constructed as an improvement over the most commonly used probe construction method. Two methods of probe calibration are presented, one at low field magnitudes in a vector network analyzer and a second method using a pulsed power Helmholtz coil. Calibration in the VNA yielded "absolute" calibration factors but tests performed in the pulsed power environment yielded variations in calibration factors of $9.7 \pm 4.6\%$ for the custom SMI probe and $12.0 \pm 3.3\%$ for the hand-wound probe relative to the VNA. Even following best practices, calibration factors for $\dot{B}$ probes are found to vary more than 20% at frequencies greater than 1 MHz relative to the two calibration methods presented.

The second journal paper presented in this dissertation addressed the temporal evolution of the energy coupling and deposition of the pulsed circuit with the inductively coupled plasma. Discharge current profiles are fit to SPICE simulations and a least squares estimate is applied to determine the plasma resistance and inductance. Simulated plasma currents are used to determine the temporal evolution of the energy coupling and losses. Three gas species are tested; argon and xenon for propulsion applications and hydrogen

to relate the results to the extensive data available in the fusion community. For prefill pressures of 10–100 mTorr, plasma resistances were found to vary from 25.8–51.6 mΩ while inductance varied from 41.3–47.0 nH. Inductively coupled energy is maximized at 3/4 of the initial discharge period. The greatest amount of energy coupled into the plasma is 6.4 J (8.4%) of the initial 79.2 $\pm$ 0.1 J. The presence of plasma results in 15.0–21.2 J (18.8–26.7%) of the initially stored energy to be ohmically dissipated through the plasma.

The final journal paper quantifies the effects of DC preionization voltage and radial location on plasma formation repeatability. Tests are conducted with argon prefill pressures of 20–200 mTorr with a discharge energy of 79.5 J at 15.0 $\pm$ 0.01 kV. SPICE simulations are fit to discharge currents; however two improvements are incorporated into the experiment to improve accuracy of results. An axial array of photomultiplier tubes are located between coil segments and provide plasma ignition and decay times. Axial imaging of the plasma and experimental geometry are used to approximate plasma thickness and thus the mutual inductance coupling of the plasma to the theta-pinch coil. Nelder-Mead simplex algorithm is incorporated into the model to minimize the error function in the least squares sense. Plasma formation was found to be impossible with the given geometry over the pressure range tested without preionization. Adding minimal PI resulted in plasma formation but yielded poor repeatability at low pressures. A DC power of 0.20 W was found to be sufficient to stabilize plasma formation at the first zero-crossing of the current while a power of 1.49 W increased inductively coupled plasma energy by 39% at 20 mTorr. For argon pressures greater than 100 mTorr, PI voltage has minimal impact on discharge repeatability. At 200 mTorr, 4.3 mW is sufficient to produce repeatable plasma formation. Radial variation of PI source had negligible affect on plasma formation properties or associated energies. These results suggest that location of PI is not as important as simply having a PI giving the experimentalist greater flexibility in experiment design.

APPENDIX

PYTHON CODES

MAKE_CIR.PY

```
###############################################################################
############################### MAKE_CIR #####################################
###############################################################################
# This function creates a netlist (.CIR) which can be ran through transient
# solver of NGSPICE. The user passes the initial conditions, circuit
# elements, and time window. If an initial current is provided, the code
# determines the appropriate current for each inductor in the circuit.
# Code writes following three values to file: time, primary current, and
# secondary voltage. No values are returned to the calling function.
#
# Input Variables:
#       V0              -       Initial voltage         [V]
#       I0              -       Initial current         [A]
#       C               -       Capacitance             [F]
#       Rp              -       Primary Resistance      [Ohm]
#       L0              -       Paras./Stray Ind.       [H]
#       Lp              -       Primary Inductance      [H]
#       M               -       Mutual Inductance       [H]
#       Ls              -       Sec./Plasma Ind.        [H]
#       Rs              -       Sec./Plasma Res.        [Ohm]
#       w               -       Discharge Freq.         [rad/s]
#       t_start         -       Start time              [s]
#       t_stop          -       Stop time               [s]
#       t_inc           -       Max time step           [s]
#
# Output Variables:
#       None
#
# Dependencies: numpy
#
def make_cir(V0, I0, C, Rp, L0, Lp, M, Ls, Rs, w, t_start, t_stop, t_inc):

        # Use T-network transformation for two inductors with a coupled
```

```
          # mutual inductance.
          LpM = Lp-M
          LsM = Ls-M

          # Deterine impedance of each secondary element.
          Z_M    = 0 + 1j*w*M
          Z_LsM  = 0 + 1j*w*LsM

          # Use current divider network to determine initial current on
          # T-network inductors.
          I0_M   = I0*np.abs(Z_LsM/(Z_LsM+Z_M))
          I0_LsM = I0*np.abs(Z_M /(Z_LsM+Z_M))

          # Create a file for writing and write each line necessary for NGSPICE
            .
          f = open("python.cir", "w")
          f.write("Simulation of complex RLC circuit based on work by Polzin (
              Ref. 101, 123) Lovberg and Dailey (Ref. 124)\n")
          f.write(" \n")
          f.write("Cp    0 1    %s IC=%s\n"    % (C, -V0))
          f.write("Rp    1 2    %s\n"          % (Rp))
          f.write("L0    2 3    %s IC=%s\n"    % (L0, I0))
          f.write("LpM   3 4    %s IC=%s\n"    % (LpM, I0))
          f.write("LM    4 0    %s IC=%s\n"    % (M,   I0_M))
          f.write("LsM   4 5    %s IC=%s\n"    % (LsM, I0_LsM))
          f.write("Rs    5 0    %s\n"          % (Rs))
          f.write(" \n")
          f.write(".options CHGTOL = 1e-16 NOPAGE NOACCT NOMOD\n") # NOPAGE
              removes extra headers that ngspace adds
          f.write(".width out = 512 \n")
          f.write(".tran %s %s %s uic\n"%(t_inc, t_stop, t_start))
          f.write(".print tran i(L0) v(5)\n")
          f.write(".end\n")
          f.close()
          return
##############################################################################
```

NGSPICE.PY

```
################################################################################
################################# NGSPICE ######################################
################################################################################
# This function reads in the netlist created by the function MAKE_CIR and
# calls NGSPICE through batch command. The output data are written to a
# .TXT file. Data are then read in and the passed secondary resistance is
# used to calculate seconday current. Three values are
#
# Input variables:
#       Rs              -       Sec./Plasma Res.       [Ohm]
#
# Dependencies: numpy, os
#
def ngspice(Rs):
        os.system('ngspice -b python.cir > python.txt')

        # Data starts on line 13.
        testdata = np.genfromtxt('python.txt',dtype='float',skip_header=12)
        t = testdata[:,1]
        Ip = testdata[:,2]
        v6 = testdata[:,3]
        Is = v6/Rs

        return t, Ip, Is
################################################################################
```

AUTO_CROP.PY

```
################################################################################
############################## AUTO_CROP ########################################
################################################################################
# This function takes an image and uses a pixel threshold to crop the image
# around the plasma. The pixel intensity defaults to 180 but can be
# overridden by a user specified value. The code then attempts to fit the
# image to a size of 315 x 315 pixels which can be overridden by a user
# specified tuple so that all images returned by this function are the same
# size. The image DPI is set by defining a final image size as a x,y tuple.
# The default image size is 315 x 315 pixels but can be overridden by a user
# defined tuple.
#
# Input Variables:
#       im              -       Python image object                      [-]
#       threshold       -       Threshold of pixel intensity [optional]    [-]
#       crop_size_px    -       Desired image size as a tuple [optional]
#                                                       [(pixel, pixel)]
#       final_size_px   -       Desired image size as a tuple [optional]
#                                                       [(pixel, pixel)]
#
# Output Variables:
#       image_resized   -       Python image object    [-]
#
# Dependencies: numpy, PIL.Image
#
def auto_crop(im, threshold = 180, crop_size_px = (315, 315), \
        final_size_px = (315, 315)):

        # Create a copy of the image. Text is added to the copied image to
        # preserve the original.
        image = im.copy()

        # Convert image to grey scale.
        grey = image.convert("L")

        # Create a transparency mask and invert. Set points that have a value
        # greater than "threshold" to "255" which is white.
        mask = Image.eval(grey, lambda(x):255-x)
        mask = mask.point(lambda i: i < threshold and 255)

        # Get the minimum and maximum pixel values
        extrema = mask.getextrema()

        # If the both the minimum and maximum pixel intensities are "0", then
        # no light was detected above the set intensity threshold. Return a
```

```
# new blank image desired image size.
if extrema[0] == 0 and extrema[1] == 0:
        print "\tImage contains no pixel luminocity. Either test had
            no plasma of the threshold is set too low."
        image_crop = Image.new("RGB", final_size_px, (0, 0, 0))

else:
        # Save mask if desired. Useful for debugging
        ##mask.save(pic_crop_dir+pic_date+pic_num+"_mask.JPG")
        ##mask.show()

        # Get boundary of mask that is not black and save in tuple
        # "box"
        box = mask.getbbox()

        # The cropped images might vary in size from test to test so
        # box may be less than intended image size "crop_size_px". If
        # the cropped region is smaller, determine how many pixels
        # needed to be added to the right AND left "delta_x" of the
        # image, and also images to be added to the top AND bottom
        # "delta_y" of the image.
        if (box[2]-box[0]) <= crop_size_px[0]:
                delta_x = (crop_size_px[0]-(box[2]-box[0]))/2.0
        else:
                delta_x = 0

        # Get number of pixels to add to image height
        if (box[3]-box[1]) <= crop_size_px[1]:
                delta_y = (crop_size_px[1]-(box[3]-box[1]))/2.0
        else:
                delta_y = 0

        # Create a new box tuple that is the same size as defined by
        # "crop_size_px".
        x0 = int(box[0] - np.floor(delta_x))
        x1 = int(box[2] + np.ceil(delta_x))
        y0 = int(box[1] - np.floor(delta_y))
        y1 = int(box[3] + np.ceil(delta_y))
        box2 = x0, y0, x1, y1

        # Crop image to new box dimensions
        image_crop = image.crop(box2)

        # Show cropped JPG image. Useful for debugging
        ##image_crop.show()

# Change image dpi
```

```
        image_resized = image_crop.resize(final_size_px, Image.ANTIALIAS)

        return image_resized
############################################################################
```

GET_M.PY

```
################################################################################
############################### GET_M ###############################
################################################################################
# This function takes in a shot number and optionally a pixel intensity
# threshold and returns plasma mutual inductance and thickness using axial
# imaging with a Canon Rebel XT. Pixel count at the given threshold are
# compared to the total possible number of pixels. This ratio is equal to
# ratio of areas which can then be used to determine thickness of plasma
# sheet.
#
# Input Variables:
#       shotnum       -        Shot number of current test              [-]
#       threshold     -        Threshold of pixel intensity [optional]  [-]
#
# Output Variables:
#       M             -        Mutual Inductance      [H]
#       t_plasma      -        Plasma Thickness       [m]
#
# Dependencies: numpy, PIL.Image
#
def GET_M(shotnum, threshold = 120):

        # Define directory where test data are stored.
        dir_data = <redacted for privacy>

        # Define directory where cropped images are stored.
        pic_dir = dir_data+"2014/05-16-2014/JPG/Auto-Cropped/"

        shotnum_str = str(shotnum)

        # Define picture name. Photos stored in the following format:
        # YYMMDDSSSS_crop.JPG
        pic_name = "140516"+shotnum_str[6:]+"_crop.JPG"

        # Open image
        image = Image.open(pic_dir+pic_name)

        # Save mask of cropped image. Useful for debugging.
        grey = image.convert("L")
        mask = Image.eval(grey, lambda(x):255-x)
        mask = mask.point(lambda i: i < threshold and 255)

        # Only top half of image is useful. Crop out lower half.
        box2 = 0, 0, 1050, 561
        mask2 = mask.crop(box2)
```

```
# Get the number of pixels in mask by converting mask to numpy array
# and using binary logic
tmp_pixels = np.asarray(mask2)
num_pixels = (tmp_pixels > 0).sum()


# Determined using Inkscape (and ruler). Out of the 1050 px wide
# image, the aluminum retaining ring has a diameter of 970 px for
# a radius of 485 px. But the solenoid obstructs the view. Using
# Inkscape, it looks the the solenoid blocks from 237 degrees to
# 347 degrees. This leaves an angle of 250 degrees
# (~1.3889*pi radians). Therefor:
#  max_num_pixels = R^2/2*(1.3889*pi).
# The retaining ring has a diameter of 5.75 in (0.14605 m)
R_aluminum_ring = 0.14605/2
max_num_pixels = 361845#517287


# Distance from vacuum chamber end-to-end is 12 ft (3.6576 m)
len_chamber = 3.6576


# Thickness of flanges is 1" (0.0254 m)
len_flange = 0.0254


# The distance from the end of the flange to MPX is 1.5" (0.0381 cm)
len_chamber_to_MPX = 0.0381


# Sensor size of the Canon Rebel Digital Camera (0.0222 m x 0.0148 m)
##camera_sensor_width = 0.0222
##camera_sensor_height = 0.0148


# Distance from camera to aluminum ring is:
# len_flange + length_chamber
# Only one flange distance is used since aluminum ring sits at front
# of north flange.
##len_camera_to_ring = len_flange+len_chamber
# based on camera sensor and geometery, about 7 cm farther than
# what was measured.
len_camera_to_ring = 3.9066


# Total length to end of MPX theta-pinch coil is:
#
# len_flange + len_chamber + len_flange + len_chamber_to_MPX
# + len_MPX_coil
#
len_total = len_flange + len_chamber + len_flange + \
        len_chamber_to_MPX + len_MPX_coil
```

```
# Radius from center of tube to beginning of plasma. Based on:
#
# A_r/A_R = [(R^2-r^2)*(theta_2-theta_1)]/[R^2*(theta_2-theta_1)]
#          = (R^2-r^2)/R^2
#  --> r^2 = R^2*(1-A_r/A_R)
#
# This is the apparent thickness of the plasma. But this is over
# exagerated due to depth of experiment into the picture. This must
# be accounted for using geometry.
r_center_to_plasma_at_ring = np.sqrt(R_aluminum_ring**2* \
        (1-1.*num_pixels/max_num_pixels))


# Once the distance from center of quartz tube to start of plasma
# radius is known, the angle this makes to the camera can be
# calculated using len_camera_to_ring:
#
# tan(theta) = r_center_to_plasma_at_ring/len_camera_to_ring
#
# The angle itself is not important but is used based on rules of
# similar triangles to determine the actual distance from center of
# quartz tube to plasma at the end of the theta-pinch coil. This will
# give an indication of total plasma thickness.
#
# tan(theta) = r_center_to_plasma_at_ring/len_camera_to_ring
#            = r_center_to_plasma_at_end/len_total
#
# and r_center to_plasma_at_end = r_quartz - r_plasma therefor solve
# for r_plasma:
# r_plasma = r_quartz - len_total*r_center_to_plasma_at_ring/
#       len_camera_to_ring
# where r_quartz = 3.04 in (7.725) cm

t_plasma = r_quartz - 1.*len_total*r_center_to_plasma_at_ring/ \
        len_camera_to_ring

# Put in a catch for dark images. If plasma thickness is less than
# zero, setthickness thickness to 1 mm
if t_plasma <= 0: t_plasma = 0.001


## Now use actual plasma thickness to calculate mutual inductance. ##
# Based on papaer of standards by Rosa and Grover. Ref 127.
#
# M = 4*pi*a^2*n1*n2*(1-2*A*alpha)
# where r = sqrt(1^2+A^2) and
# alpha = (A-r+1)/(2*A)-(a^2)/(16*A^2)*(1-A^3/r^3)
#             -(a^4)/(64*A^4)*(1/2+2*A^5/r^5-5/2*A^7/r^7)
```

```
#
# Use the averate plamsa radius: a = r_plasma_avg = r_quartz-
# t_plasma/2
#
a = r_quartz-t_plasma/2


# Turn density of theta pinch coil [turns/cm]
n1 = 1/len_MPX_coil


# Turn density of plasma; assumed to be same length as theta pinch
# [turns/cm]
n2 = 1/len_MPX_coil


# Inner radius of theta pinch; assumed to be radius of primary
    inductor [cm]
A = 0.1778/2


# Distance parameter used in Rosa and Grover
r = np.sqrt(len_MPX_coil**2+A**2);


# Magnetic Permeability of free space [H/m]
u0 = 4*np.pi*1e-7


alpha = (A-r+len_MPX_coil)/(2*A)-(a**2)/(16*A**2)* \
                (1-np.power(A, 3)/np.power(r, 3)) - \
                (np.power(a, 4))/(64*np.power(A, 4))* \
                (1/2+2*np.power(A, 5)/np.power(r, 5) - \
                5/2*np.power(A, 7)/np.power(r, 7));


M = u0*np.pi*a**2*n1*n2*((len_MPX_coil-2*A*alpha))


# Return mutual inductance and plasma thichness. Convert plasma
# thickness to [m] since the rest of the code uses mks units.
return M, t_plasma
###############################################################################
```

FILTER_RYAN.PY

```
################################################################################
############################## FILTER_RYAN #####################################
################################################################################
# This function takes in an array and applies a filter operation. The
# Buttord method is used to generate the necessary parameters for a
# butterworth filter with the desired characteristics. The function defaults
# to a low-pass filter but the user can manually specify band pass
# frequency, stop band frequency, max ripple, attenuation at stop band, and
# filter type.
#
# Input Variables:
#       shotnum         -       Shot number of current test               [-]
#       threshold       -       Threshold of pixel intensity [optional]    [-]
#       plot            -       Boolean. If '1', plot results. [optional]  [-]
#       Wp              -       Pass band frequency [optional]        [rad/s]
#       Ws              -       Stop band frequency [optional]        [rad/s]
#       gpass           -       Max ripple in pass band [optional]         [dB]
#       gstop           -       Attenuation at stop band [optional]        [dB]
#       filt_type       -       Type of filter to apply [optional]         [-]
#
# Output Variables:
#       data_filt       -       Filtered data  [-]
#
# Dependencies: numpy.array, scipy.signal
#
def filter_ryan(data, sample_rate = 60e6, Wp = 5e6, Ws = 10e6, gpass = 3, \
        gstop = 40, filt_type = 'low'):

        from scipy import signal
        from numpy import array

        # Read in data and convert to numpy array.
        data = array(data, dtype = float)

        # Read in sample rate and convert to integer.
        sample_rate = int(sample_rate)

        # Nyquist frequency
        nyquist = sample_rate/2

        # Read in and convert pass band (rad/s) to float.
        Wp = float(Wp)

        # Read in and convert stop band (rad/s) to float.
        Ws = float(Ws)
```

```
# Read in and convert pass band allowed ripple (dB) to float.
gpass = float(gpass)

# Read in and convert stop band attenuation ripple (dB) to float.
gstop = float(gstop)

# Use scipy's buttord to determine order and normalized frequency to
# be then feed into butterworth filter.
N, Wn = signal.buttord(Wp/nyquist, Ws/nyquist, gpass, gstop)

# Use scipy's butterworth filter to generate filter coefficients.
b, a = signal.butter(N, Wn, filt_type)

# Use scipy's filtfilt function to do a forward and backward filter
# using the b and a coefficients fround from butterworth filter. The
# filtfilt filter should not produce any phase delay.
data_filt = signal.filtfilt(b, a, data)

return data_filt
```

FIND_PEAKS.PY

```
##############################################################################
############################## FIND_PEAKS #############################
##############################################################################
# This function attemps to determine the peaks and troughs of corresponding
# to the data passed to it.
# Filter settings
#
# Input Variables:
#       current_data    -       Array of data, typically discharge current [-]
#       num_pks         -       Number of peaks to find     [optional]    [-]
#       plotter         -       Boolean. If '1', plot results. [optional]  [-]
#       sample_rate     -       Sample rate of DAQ system [optional] [Sample/s]
#
# Output Variables:
#       tmp_idx -       Array of indices corresponding to peaks and troughs of
#                               current_data [-]
#
# Dependencies: numpy, filter_ryan, matplotlib.pyplot
#
def find_peaks(current_data, num_pks = 20, plotter = 0, sample_rate = 60e6):
        stop_interval = num_pks

        # Define filter settings
        Wp = 10e6               # Pass band                     [rad/s]
        Ws = 15e6               # Stop band                     [rad/s]
        gpass = 3               # Maximum ripple in pass band       [db]
        gstop = 40              # Attenuation in stop band          [dB]
        filt_type = 'low'     # Type of filter                  [-]

        # Apply low-pass filter to data
        current_data_filt = filter_ryan(current_data, \
                sample_rate = sample_rate, Wp = Wp, Ws = Ws, \
                gpass = gpass, gstop = gstop, filt_type = filt_type)

        # Create empty array to store indices
        tmp_idx = np.zeros((stop_interval+1, ), dtype = int)
        for j in range(0, stop_interval):
                tmp_idx[j+1] = tmp_idx[j]+(np.power(-1, j)* \
                        current_data_filt[tmp_idx[j]:]).argmax()

        # Plot if flag is true
        if plotter:
                fig, ax = plt.subplots()
                ax.plot(range(0,len(current_data)), current_data, 'k', \
                label = 'Original Data')
```

```python
            ax.plot(range(0,len(current_data_filt)), current_data_filt, \
            'b', label = 'Filtered Data')
            ax.plot(tmp_idx, current_data_filt[tmp_idx], 'ro', \
            label = 'Peaks')
            ax.legend(loc = 'best', shadow = True)
            plt.show()

        # Return the indices of the peaks/troughs
        return tmp_idx[1:]
################################################################################
```

FFT_RYAN.PY

```
################################################################################
############################### NGSPICE ###############################
################################################################################
# This function takes in an array of points and performs a fast-Fourier
# transform (FFT) on the data. The program returns the FFT of the data and
# the corresponding frequency range.
#
# Input variables:
#      data           -       Array of points        [-]
#      smaple_rate    -       Sampling rate of DAQ  [Sample/s]
#
# Output Variables:
#      xf             -       Array of frequency values                 [Hz]
#      yf             -       Array of points corresponding to FFT(data) [-]
#
# Dependencies: scipy.fftpack.fft, numpy.array, np.linspace, np.abs
#
def fft_ryan(data, sample_rate = 60e6):
        from scipy.fftpack import fft
        from numpy import array, linspace, abs

        # Convert data to numpy array
        y = array(data, dtype = float)
        sample_rate = int(sample_rate)

        # Number of samples
        N = len(y)

        # Take FFT
        yf = fft(y)

        # Since returned array is symmeric, take only last half of array
        yf = 2.0/N * abs(yf[0:N/2])

        # Calculate frequency data
        xf = linspace(0.0, sample_rate/2, N/2.0)

        return xf, yf
################################################################################
```

CIRCUIT_MODELING.PY

```
###############################################################################
######################### CIRCUIT_MODELING ############################
###############################################################################
# This function determines the interval of the discharge current where
# plasma is present and attemps to fit the discharge current waveform using
# SPICE simulation. The Nelder-Mead Simplex method is applied to the
# resulging error function to determine the circuit parameters that best
# approximate the plasma discharge.
#
# Input Variables:
#      shotnum        -       Shot number of current test                [-]
#      threshold      -       Threshold of pixel intensity [optional]    [-]
#      plot           -       Boolean. If '1', plot results. [optional]  [-]
#
# Output Variables:
#      None
#
# Dependencies: numpy, PIL.Image, GET_M, filter_ryan, find_peaks,
#               MDSPlus.Tree, MDSPlus.Data, make_cir, ngspice,
#               scipy.interpolate.InterpolatedUnivariateSpline,
#               scipy.interpolate.interp1d,
#               scipy.optimize.fmin, matplotlib.pyplot
#
def Circuit_Modeling(shotnum, threshold = 120, plot = 0):
        print "Shotnum:", shotnum, "\nThreshold:", threshold
        print "Plasma interval: %s - %s" % plasma_interval[shotnum]

        # Define discharge capacitor capacitance [F]
        C = 707e-9

        # Define vacuum shots. The first three tests ('0000', '0001', and
        # '0002') were intensional vacuum shots; however three tests at 20
        # mTorr failed to produce plasma: ('0019', '0020', and '0021').
        if shotnum in [1405160000, 1405160001, 1405160002, 1405160019, \
                            1405160020, 1405160021]:
                M = 0
                t_plasma = 0
        else:
                M, t_plasma = GET_M(shotnum, threshold)

        # Primary (theta-pinch) inductance. Determined from
        # Ref. 045 [Lundin].
        Lp = 36.24e-9                    #        [H]

        # Parasitic/stray inductance. Determined from fitting vacuum
```

```
# discharge current to simple RLC circuit model and subtracting
# primary inductance.
L0 = 185.078683333e-09-Lp      #        [H]


# Primary circuit series resistance. Determined from
# fitting vacuum discharge current to simple RLC circuit
# model.
Rp = 0.0403857165333           #        [Ohm]


# Time step between data points acquired by PXI-5105 DAQ cards
# with a sampling rate of 60 MS/s .
dt = 1/60e6                     #        [s]


# Data are stored using MDSplus data structure (mdsplus.org). Read
# in data as "ReadOnly" to protect original data.
tree = Tree(tree_name, shotnum, "ReadOnly")


# Retrieve necessary data from MDSplus tree.
pressure        = tree.getNode('\PRESSURE').data()
pi_rogo         = tree.getNode('\PI_ROGO:CAL_SIG')
num_pts         = tree.getNode('\PI_ROGO:NUM_PTS').data()
sample_rate     = tree.getNode('\PI_ROGO:SAMPLE_RATE').data()
dt              = tree.getNode('\PI_ROGO:TIME_STEP').data()


# Need to average all eight PMT channels to get global plasma
# ignition time. Preallocate space and read in each channel.
pmt_sum = np.zeros((pi_rogo.data().size), dtype=float)
for j in range(1,9):
        pmt_sum = pmt_sum+tree.getNode('\PMT_%i:CAL_SIG' % j).data()


# Filter PMT data using a low-pass filter.
pmt_sum_filt = filter_ryan(pmt_sum, \
        sample_rate = sample_rate, Wp = Wp, Ws = Ws, \
        gpass = gpass, gstop = gstop, filt_type = filt_type)


# Filter Current data so that peaks are easier to find.
current_filt = filter_ryan(pi_rogo.data(), \
        sample_rate = sample_rate, Wp = Wp, Ws = Ws, \
        gpass = gpass, gstop = gstop, filt_type = filt_type)


# Find peaks/troughs of filtered current data. Need to go one past
# the last value since this code uses peaks of current, not zero
# crosses.
peaks = find_peaks(current_filt, int(plasma_interval[shotnum][1])+1)


# The time region of interest is indicated by 'plasma_interval'. Use
# this interval and the peak data to bracket the current waveform
```

```
# which is then used with ngspice model. Interval data saved in CSV
# file: "Plasma_interval.csv".
filehandle = open("Plasma_interval.csv", "r")
plasma_interval = dict()

for line in filehandle:
line_entries = line.split(",")
plasma_interval[int(line_entries[0])] = \
        (line_entries[1], line_entries[2])

if int(plasma_interval[shotnum][0]) == 0:
        idx_start = peaks[int(plasma_interval[shotnum][0])]
else:
        idx_start = peaks[int(plasma_interval[shotnum][0])-1]

idx_stop = peaks[int(plasma_interval[shotnum][1])]

# Get subset of time and current corresponding to PMT activity.
time = pi_rogo.dim_of().data()[idx_start:idx_stop]- \
        pi_rogo.dim_of().data()[idx_start]
current = pi_rogo.data()[idx_start:idx_stop]

# Find ideces of 'time' that will give the first and last zero
# crossings of the current which correspond to plasma activity
# based on PMT signals. Spice simuations are still done from
# current peak prior first zero cross through the current peak
# after the last zero cross. The LSE uses the time bracket
# associated with 't0_first' and 't0_last' which better
# correspond to plasma activity.
t0_first = np.abs(pi_rogo.data()[peaks[0]:peaks[1]]).argmin()
t0_last = np.abs(pi_rogo.data()[peaks[-2]:peaks[-1]]).argmin() + \
        (peaks[-2]-peaks[0])

# Peak current
I0 = current[0]

# Determine center frequency of discharge using FFT. Pad with zeros
# if necessary to get desired resolution. With 18,000 data points,
# frequency resuloution is ~3.3 kHz. With a padding of 2^3*num_pts,
# resolution improves to ~0.4 kHz or ~0.2 kHz at 2^4 num_pts.
tmp = np.zeros((np.power(2,4)*num_pts), dtype = float)
tmp[:len(time)] = current
freq, yf = fft_ryan(tmp)
w = 2*np.pi*freq[yf.argmax()]

# The Nelder-Mead method called by fmin requires a function to
# evaluate. This subfunction takes in the current guess 'X' which is
```

```python
# an array containing the secondary resistance and inductance and
# returns the sum of squares of the residuals (error). This function
# will call "make_cir" to create a netlist and then "ngspice" to
# evaluate the netlist and carry out the simulation in SPICE.
def Z(X):
        Rs = X[0]        #         [Ohm]
        Ls = X[1]        #         [H]

        make_cir(0, I0, C, Rp, L0, Lp, M, Ls, Rs, w, time[0], \
                time[-1], t_inc = dt)
        t, Ip, Is = ngspice(Rs)

        # Linearly intertopate function. Caution: interp1d can not
        # extrapolate values. Using InterpolatedUnivariateSpline
        # instead. The SPICE code will sometimes produce time arrays
        # that will not let it be linearly interpolated with the time
        # array without some extrapolation required.
        order = 1
        s = InterpolatedUnivariateSpline(t, Ip, k=order)
        i_guess = s(time)

        # ngspice starts current at zero to account for transients.
        # For the purposes of this code, it needs to start at
        # I0 = I_max otherwise there is significant error on the
        # first point. Therefore, set the first value of the
        # simulated current equal to the second value so that it
        # starts at a non-zero value.
        i_guess[0] = i_guess[1]

        Z = np.sum(((i_guess[t0_first:t0_last] - \
                current[t0_first:t0_last])/ \
                len(i_guess[t0_first:t0_last]))**2)

        return Z

# Use a simple RLC circuit for vacuum tests.
if pressure < 5:
        ii = shotnum-1405160000

        # Time at which discharge current has returned to zero.
        t_end = 30e-6 #        [s]
        idx_zero = np.abs(pi_rogo.dim_of().data()-0).argmin()
        idx_end = np.abs(pi_rogo.dim_of().data()-t_end).argmin()

        # To fit the vacuum cases, need to shift current data to get
        # rid of initial negative pulse.
        # This section of code was manually extracted by plotting
```

```python
# individual tests and determining offset values.
#       0000: -1.718e-7 [s]
#       0001: -1.711e-7 [s]
#       0002: -2.026e-7 [s]
vac_offset = (1.718e-7, 1.711e-7, 2.026e-7)
t_tmp   = pi_rogo.dim_of().data()[idx_zero:idx_end+1] - \
        vac_offset[ii]
i_actual = pi_rogo.data()[idx_zero:idx_end+1]
V0 = tree.getNode('\PI_VOLT').data()*1e3


# The Nelder-Mead method called by fmin requires a function to
# evaluate. This subfunction takes in the current guess 'X'
# which is an array containing the series resistance and
# inductance and returns the sum of squares of the residuals
# (error) using an analytical solution of a series RLC
# circuit.
def Z_RLC (X):
        R = X[0]        # [Ohm]
        L = X[1]        # [H]

        # Discharge freqency [rad/s]
        Wn_guess = np.sqrt(1/(L*C)-(R/(2*L))**2)
        i_guess = V0/(Wn_guess*L)*np.exp(-(R*t_tmp)/(2*L))* \
                np.sin(Wn_guess*t_tmp)

        Z_RLC = np.sum((i_guess-i_actual)**2)

        return Z_RLC


# Use Nelder-Mead Simplex method to determine circuit values
# that best match discharge current in least squares sense.
X0 = [50e-3, 180e-9]
xopt = fmin(Z_RLC, X0, ftol=1e6, xtol=1e-6, maxiter=200, \
        maxfun=400)
print "\nR:\t%1.3f mOhm\nL:\t%1.3f nH\n" % \
        (xopt[0]*1e3, xopt[1]*1e9)


Rp = R = xopt[0]
L = xopt[1]
L0 = L-Lp


# Create a tuple of circuit parameters:
#       (C, Rp, L0, Lp, M, Ls, Rs, t_plasma, error)
circuit_params = (C, Rp, L0, Lp, 0, 1e6, 1e6, 0, Z(xopt))

Wn_guess = np.sqrt(1/(L*C)-(R/(2*L))**2)
i_guess = V0/(Wn_guess*L)*np.exp(-(R*t_tmp)/(2*L))* \
```

```
                        np.sin(Wn_guess*t_tmp)


            # Create an expression for the time array.
            expr_time = Data.compile( \
                    "MAKE_RANGE($1, ($2-1)*$3+($1), $3)", t_tmp[0] + \
                    vac_offset[ii], len(t_tmp), dt)

            # Set secondary current to zero since there is no plasma on
            # vacuum shots.
            Ip = i_guess
            Is = np.zeros((t_tmp.shape), dtype = int)

            # If boolean flag 'plot' is true, plot simulated current vs.
            # recorded discharge current
            if plot:
                    R = xopt[0]
                    L = xopt[1]
                    Wn_guess = np.sqrt(1/(L*C)-(R/(2*L))**2)
                    i_guess = V0/(Wn_guess*L)*np.exp(-(R*t_tmp)/(2*L))* \
                            np.sin(Wn_guess*t_tmp)
                    plt.plot(t_tmp, i_actual, 'k', t_tmp, i_guess, 'r')
                    plt.show()


# If not a vacuum test, use Nelder-Mead simplex method and iterate
# through plasma resistance and inductance values with SPICE
# simulations.
else:
        X0 = [10e-3, 45e-9]

        xopt = fmin(Z, X0, ftol = 1e2, xtol = 1e-6, maxiter = 200, \
        maxfun = 400)

        Rs = xopt[0]
        Ls = xopt[1]

        print "\nRs:\t%1.3f mOhm\nLs:\t%1.3f nH\n" % \
                (xopt[0]*1e3, xopt[1]*1e9)

        # Re-run once more to get current data for the calculated
        # circuit parameters.
        make_cir(0, I0, C, Rp, L0, Lp, M, Ls, Rs, w, time[0], \
                time[-1], t_inc = dt)
        t, Ip, Is = ngspice(Rs)

        # Use linear interpolation to match SPICE time base with
```

```
# measured data time base.
f  = interp1d(t, Ip, kind = 'linear', axis = -1, \
        copy = True, bounds_error = True, fill_value = np.nan)
f2 = interp1d(t, Is, kind = 'linear', axis = -1, \
        copy = True, bounds_error = True, fill_value = np.nan)


# Round-off error will sometimes result in time[-1] > t[-1]
# by ~1e-12. If this occurs, and error is small, set the last
# time point equal to the last time point in the simulation
# and try again.
try:
        ip_guess = f(time)
        is_guess = f2(time)
except:
        if time[-1]-t[-1] <= 1e-11:  time[-1] = t[-1]


        ip_guess = f(time)
        is_guess = f2(time)


# SPICE always returns an initial value of zero which is not
# physical. Set initial value to the second value in array.
ip_guess[0] = ip_guess[1]
is_guess[0] = is_guess[1]


Ip = ip_guess
Is = is_guess


# Create a tuple of circuit parameters:
#       (C, Rp, L0, Lp, M, Ls, Rs, t_plasma, error)
circuit_params = (C, Rp, L0, Lp, M, Ls, Rs, t_plasma, Z(xopt))


# Create an expression for the time array
expr_time = Data.compile( \
"MAKE_RANGE($1, ($2-1)*$3+($1), $3)", \
        time[0]+pi_rogo.dim_of().data()[idx_start], \
        len(ip_guess), dt)


# If boolean flag 'plot' is true, plot simulated current vs.
# recorded discharge current
if plot:
        fig, ax = plt.subplots()
        ax.plot(pi_rogo.dim_of().data(), pi_rogo.data(), 'k', \
                label = 'PI Rogo')
        ax.plot(time[t0_first:t0_last] + \
                pi_rogo.dim_of().data()[idx_start], \
                current[t0_first:t0_last], 'm', \
                label='Plasma Interval')
```

```
        ax.plot(time+pi_rogo.dim_of().data()[idx_start], Ip, \
                'r', label='Ip')
        ax.plot(time+pi_rogo.dim_of().data()[idx_start], Is, \
                'b', label='Is')
        ax.plot(pi_rogo.dim_of().data(), \
                pmt_sum_filt/np.max(pmt_sum_filt)*I0, 'g', \
                label='Summed PMTs')

        ax.legend(loc='best', shadow = True)
        ax.axis([-1e-6, 30e-6, -25e3, 30e3])
        plt.show()

    return 1
###########################################################################
```

VITA

Ryan Pahl was born in 1987 in St. Louis, Missouri and later raised in Eureka, Missouri. Ryan attended Eureka High School graduating in 2005 and enrolled at Missouri University of Science and Technology (then University of Missouri-Rolla) where he pursued a bachelors degree in Aerospace Engineering. Ryan completed his BS in May 2008 having taken only three years.

Ryan received his Masters in Aerospace engineering from Missouri S&T in May 2010. For his MS, Ryan investigated a refrigerant-based cold-gas propulsion system designed for small student satellites. Ryan received the Academy of Mechanical and Aerospace Engineer's Student Excellence Award for his work on the Missouri Satellite Team. He placed 1st in the 2010 Frank J. Reid Student paper competition along with his co-author Christopher Tutza at the 24th AIAA/USU Small Satellite Conference.

Following his interest in spacecraft propulsion, Ryan joined the Aerospace Plasma Laboratory under Dr. Joshua Rovey. Ryan completed his PhD in Aerospace Engineering in December 2014 having investigated the use of a ringing theta-pinch device for energy deposition into a pulsed inductive plasma.